Electrical conductivity of single Be-doped GaAs nanowires

Relatore:

Prof. Federico Boscherini

Presentata da:

Eleonora Spurio

Correlatore:

Prof. Dr. Ullrich Pietsch
Dr. Danial Bahrami

Abstact

In this thesis the measurement of the current-voltage characteristics of single nanowires in their as-grown geometry is presented. The studied sample is composed by Be-doped GaAs nanowires grown on Si substrate by molecular beam epitaxy. The measurements have been performed using the two terminal and the four terminal geometry, respectively in the laboratories of *Universität Siegen* and of *Leibniz Universität Hannover*.

For applications of nanowires in optoelectonic applications the profound knowledge of electronic properties is fundamental for device optimization. The first aim of this work is the investigation of electric properties of individual nanowires onto the same substrate. The electrical characterization has been performed measuring the current-voltage characteristics of single nanowires in the two-terminal and four-terminal geometry. The resistance of single nanowires onto the same substrate has been calculated by fitting the obtained characteristics using *thermionic emission theory*. The obtained values are strongly different from nanowire to nanowire, meaning differences in conductivity of nanowires on the same substrate.

Then, the resistance profile along single nanowires has been measured in the two-terminal configuration. This measurement shows a quasi-exponential decrease in nanowire conductivity from the bottom to the top part of individual nanowires. The experimental results are in good agreement with numerical simulations obtained using *Finite Element Method* calculations.

The correct implantation of nanowires onto real devices also requires the knowledge of the correlation between the mechanical stress applied to single nanowires and their electric properties. The analysis of this correlation has been performed using the two terminal configuration, by applying different mechanical stress to the same nanowire and measuring the current-voltage characteristic at each step. The results show an increase in conductivity of the single nanowire with the increase of the applied tension.

Sommario

In questa tesi viene presentata la misura della caratteristica corrente-tensione di singoli nanofili nella loro configurazione di crescita. Il campione studiato è composto da nanofili di GaAs drogati con Be cresciuti su un substrato di Si tramite epitassia di fasci molecolari. Le misure sono state effettuate utilizzando la configurazione a due contatti e a quattro contatti, rispettivamente all'interno dei laboratori di *Universität Siegen* e di *Leibniz Universität Hannover*.

Per l'utilizzo dei nanofili in applicazioni optoelettroniche, è fondamentale conoscere a fondo le proprietà elettriche per l'ottimizzazione dei dispositivi. Il primo obiettivo di questo lavoro è l'analisi delle proprietà elettriche dei singoli nanofili sullo stesso substrato. La caratterizzazione elettrica è stata ottenuta misurando la caratteristica corrente-tensione dei singoli nanofili nella configurazione a due e a quattro contatti. La resistenza dei singoli nanofili sullo stesso substrato è stata calcolata fittando le curve caratteristiche misurate con la teoria di emissione termoionica. I valori ottenuti sono fortemente diversi da nanofilo a nanofilo, implicando differenze nella conduttività dei nanofili sullo stesso substrato.

In seguito, si è anche misurato il profilo di resistenza lungo i singoli nanofili, utilizzando la configurazione a due terminali. Questa misura mostra un decadimento quasi esponenziale nella conduttività dei nanofili dal fondo alla cima del singolo nanofilo. I risultati sperimentali sono in buon accordo con le simulazioni numeriche ottenute utilizzando il Metodo degli Elementi Finiti.

Il corretto impianto dei nanofili su dispositivi reali richiede anche la conoscenza della correlazione fra stress meccanico e proprietà elettriche. L'analisi di questa correlazione è stata effettuata utilizzando la configurazione a due terminali, applicando diversi gradi di stress allo stesso nanofilo e misurando la caratteristica corrente-tensione ad ogni passo. I risultati mostrano una crescita della conduttività del singolo nanofilo con l'aumento della tensione applicata.

Contents

Acronyms

AFM Atomic Force Microscopy
C-AFM Conductive Atomic Force Microscopy
CB Conduction Band
CMOS Complementary metal-oxide semiconductor
CVD Chemical Vapor Deposition
EBL Electron Beam Lithography
FE Field Emission theory
FEM Finite Element Method
FET Field-Effect Transistor
FIB Focused Ion Beam
IBL Ion Beam Lithography
I-V Current-Voltage
LED Light Emitting Diode
LPE Liquid Phase Epitaxy
MBE Molecular Beam Epitaxy
MS Metal/Semiconductor
NW Nanowire
OLED Organic Light Emitting Diode
SEM Scanning Electron Microscopy
SF Stacking Fault
STM Scanning Tunneling Microscopy
UHV Ultra-High Vacuum
VB Valence Band
VLS Vapor-Liquid-Solid
WZ Wurtzite
ZB Zinc-blende

Introduction

Nanowires (NWs) are nanostructures with an aspect ratio (i.e. length over diameter ratio) larger than 1000. Typically, NW diameters are of the order of some hundreds of nanometers: at this scale, quantum mechanical effects are important and NWs behaviour is different with respect to their bulk counterpart. This gives to NWs unique physical properties, which are interesting for a large number of possible applications. NWs can be obtained through advanced growth methods and they exist in many forms: made of metals, semiconductors, insulators and organic compounds. In this thesis, semiconductor NWs will be investigated.

Semiconductor NWs have been employed as LEDs, transistors, anti-reflective coating and can potentially increase efficiency of devices based upon bulk materials e.g. in photonics [1], energy storage [2], bio-sensing [3] and high-speed electronics [4].

For profound understanding of future NW applications, it is important to study how electrical properties of single semiconductor NW are affecting the NW performances. Previously, it has been shown that the electrical resistance of single GaAs NWs depends on the number of axial interfaces along the NW growth axis [5]. The most common method to investigate electrical properties of single NWs is the FET configuration. Here the NWs are removed from the original growing substrate and later deposited onto an insulating substrate. Their electrical properties are studied using the single NWs as the semiconductor channel of the FET. Here, in this thesis, I am characterizing single free-standing NWs on their growing substrate, using W-needles in a two- and four-terminal geometry. This technique is more uncommon, but in several aspects superior, to the characterization of NWs in the FET configuration.

Sharp metallic probes with precisely controlled position can be employed to approach single semiconductor NWs in their as-grown geometry. FIB/SEM dual beam system is used to perform two-point electrical conductivity measurements and STM/SEM system is employed for four-point electrical conductivity measurements.

In the first chapter of this thesis the semiconductor NWs growth methods, their crystal structure and their applications are described. In the second chapter, the experimental methods for electrical characterization of semiconductor NWs, as well as the theoretical models of these measurements are presented. The third chapter describes the experimental setup employed for electrical measurements and the FEM, used for

numerical simulations. At the beginning of the fourth chapter, the sample type and experimental setup for the two-point contact measurements are presented. Then, the electrical resistance of single NWs on the same substrate is extracted, and the current map along one single NW and the conductivity of single NWs under applied mechanical stress are studied. The fifth chapter describes the four-points electrical conductivity measurements, together with the challenges and of the limitations faced in this configuration. Finally, I discuss the obtained results from electrical conductivity measurements on single GaAs NWs in their as-grown geometry.

Chapter 1

Semiconductor nanowires

Nanowires (NWs) are slender structures that are only a few billionths of a meter in diameter but many thousands or millions of times longer. The MIT professor Silvija Gradeĉak describes NWs as quasi one-dimensional materials, with two of their dimensions in the nanometer scale. Quantum confinement gives to these nanostructures distinctive electrical and optical properties [6].

Growth processes must be able to preferentially support growth in one dimension [7]. In chapter 1, the techniques of gold assisted growth and self-assisted growth of III-V semiconductor NWs are described. Growth can take place either randomly on the substrate or on pre-defined locations (selective area growth). The crystalline structure of GaAs NWs is described. Then, some of the possible applications of NWs are presented, based mainly on GaAs NWs, with examples referred to already existing devices. In the end, the physics of GaAs at the nanoscale is investigated, mainly focused on electrical and optical properties of GaAs NWs.

1.1   Epitaxial nanowire growth

Semiconductor and metallic NWs can be obtained both via top-down etching or bottom up approach. Top-down methods use bulk materials of desired composition, and achieve nanoscale dimensions by lithographic techniques that essentially carve the desired structure out of the material. Even if this is a very common technique for material processing, as the desired length scales of devices and applications shrink, this technique becomes more problematic [8]. More importantly, using top-down approach is difficult to control quality of structures [9]. On the other hand, bottom-up methods are based upon self-assembling atoms to form increasingly larger structures. The most common technique for the growth of NWs is the so called vapour-liquid-solid (VLS) mechanism. It was established in the 1960s by Wagner et al.[10], to grow one dimensional Si whisker-like structures.

1.1.1   Gold assisted growth

The first growth technique for NWs was based upon the use of a metal particle (typically Au) as catalyst for the NW formation. The growth process is schematized in figure 1.1. First, a thin layer of Au is deposited onto the substrate and annealed above the melting temperature, leading to the formation of Au droplets (a). After, the temperature of the substrate is adjusted to the desired growth temperature (typically several hundreds of °C), and atoms of the growing species (e.g. Ga and As) are supplied through the vapor phase (b). Au particles act as the preferential sites for the nucleation of the NW growth: both Ga and As components become oversaturated in the liquid droplet. At this point, the condensation of the vapour species and the precipitation of a solid phase at the particle-substrate interface takes place (c). In mononuclear approximation the nucleation process occurs at the boundary between the droplet and the NW top. This can start in two different positions: at the center or close to the outer surface of the droplet [11]. The diameter of the resulting NWs directly depends on the size of the catalyst droplet.
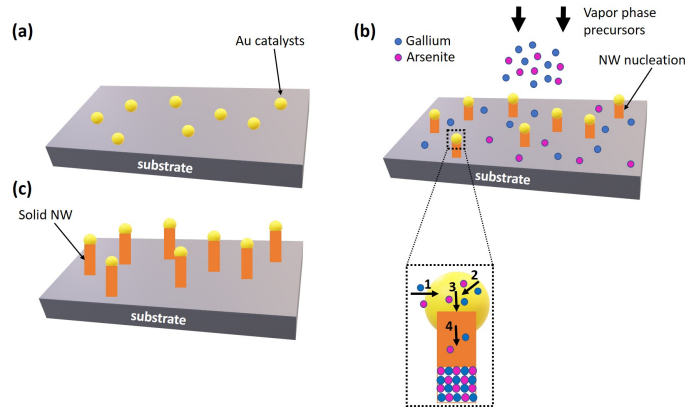
Figure 1.1: Schematic illustration of the Au-assisted VLS growth mechanism and III-V compound semiconductor NWs growth. (a) Metal catalytic particles (Au) are deposited onto the substrate and, at elevated temperatures, they form alloy droplets with the substrate material. (b) As vapour-phase precursor molecules (Ga and As) are continuously supplied, Au droplets become supersaturated and (c) eventually act as nucleation sites for NW crystal growth.

Although the growth scheme using Au-particles as sketched above is highly successful, it presents some strong limitations for practical applications. In particular, Au catalysts are incompatible with Si based devices and standard CMOS technology. Some Au particles diffuse within Si, creating defects that trap electrons and holes in Si [12]. Furthermore, it has been observed by Breuer S. et al. [13] that the minority carrier lifetime for the Au-assisted NWs is more than 2 orders of magnitude shorter than the

expectations for state-of-the-art material quality. This drastic quenching is due to the non-negligible incorporation of Au, an efficient nonradiative center, into NWs grown under the assistance of Au droplets.

1.1.2 Self-assisted growth

In the self-assisted growth, also known as Ga-assisted growth, a Ga droplet acts as a catalyst for NW growth. This was first demonstrated by Fontcuberta et al.[14] and by Colombo et al.[15] on an oxide covered GaAs surface. The process is illustrated in figure 1.2.
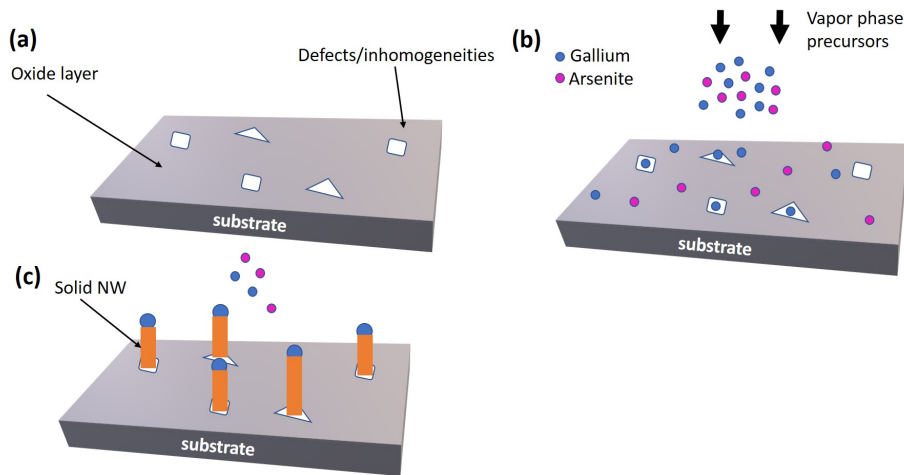
Figure 1.2: Schematic representation of the Ga-assisted growth of GaAs NWs. (a) Growth is initiated on an substrate covered by a thin oxide layer, that can be a native oxide or an artificially deposited layer. (b) If Ga and As are supplied in the vapor phase, Ga droplets form on the surface and bond to defects or inhomogeneities in the oxide layer. (c) VLS growth leads to the formation of GaAs NWs.

In a first step, the substrate is covered by a thin oxide layer (a). This oxide layer can either be the native oxide, for example in the case of a Si substrate, or may be deposited by thermal or chemical treatment of the surface. In a next step, Ga and As are supplied in the growth chamber at the desired growth temperature (b). Whereas As initially desorbs from the surface, Ga atoms can accumulate and form droplets, pinned at defects within the surface layer and occurring at random positions. At these positions, Ga can partially dissolve the oxide layer, leading to a direct contact with the underlying substrate, on which heteroepitaxial growth can start (c). This growth scheme naturally avoids a possible incorporation of impurity atoms into the NW, as no other atoms are present during growth.

The oxide layer is a key parameter of growth, as shown in the works by Madsen et al. [16] and by Matteini et al. [17]: its thickness and stoichiometry influence qualities like number density and tilting of the NWs.

1.1.3   Selective area growth

In the growth processes described above, the aggregation of droplets and the location of NWs is randomly distributed on the substrate. However, for practical applications it is more convenient to have a systematic order of the NW arrays. To deposit NWs with a pre-defined pattern, the catalysed growth is substituted by a side-selective growth on a substrate that is partially covered by a mask, on which no growth occurs (figure 1.3). GaAs NWs can be grown using selective-area metal-organic vapor phase epitaxy (MOVPE) throughout holes in a SiO_x or SiN_x layer, that has been patterned by EBL or by IBL and etching of small openings in the oxide layer.

This technique allows to obtain GaAs NWs which are position-controlled and vertically aligned [18]. The yield of NWs is controlled by Ga predeposition time, As flux, and substrate annealing treatment. [19].
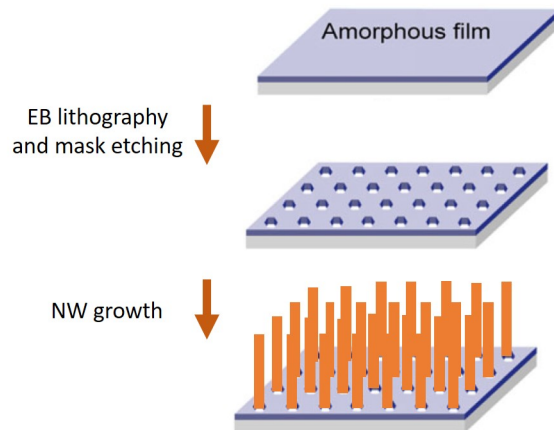
Figure 1.3: Fabrication process for selective-area MOVPE. After the amorphous film is deposited, hole openings are formed by lithography and etching. NWs are grown by MOVPE.

1.2   Crystal Structure of GaAs nanowires

Crystalline structure is defined by a repeating, three dimensional pattern of atoms (or molecules) with a fixed distance between the constituent parts. A change in the crystal lattice will thus change the crystal structure. The most common crystalline phases

(a) ZB structure.　　　　　　　　(b) WZ structure.
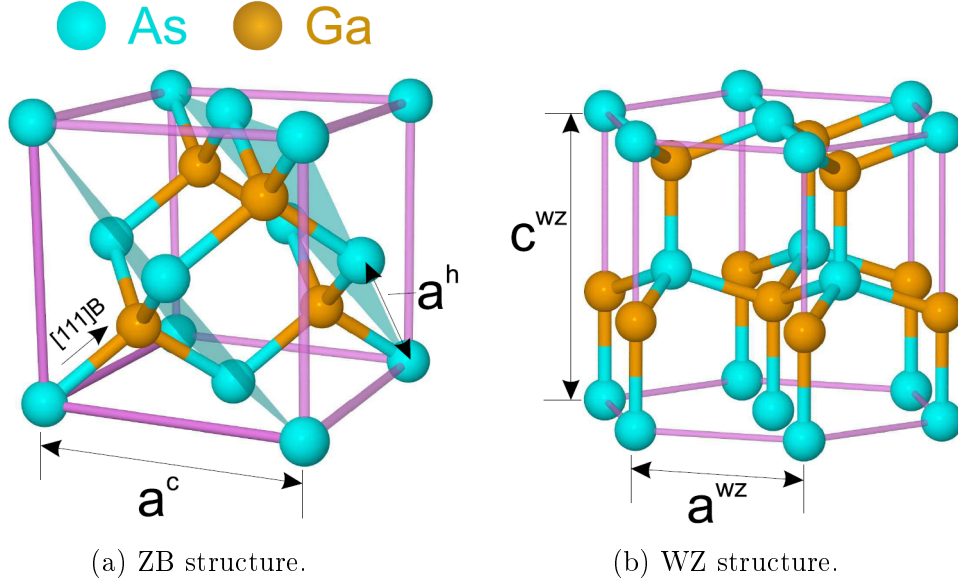
Figure 1.4: In the ZB lattice (a), both fcc lattices are occupied by different atoms, e.g. Ga and As. The structure can be thought of as bilayers of Ga-As stacked in a sequence ABCABC... . The hexagonal wurtzite structure (b) is build from bilayers stacked in a sequence ABAB...[12] .

of group III-V semiconductors are the cubic zincblende (ZB) phase and the hexagonal wurtzite (WZ) phase [20]. GaAs (as the most of III-V materials, except for the Group III nitrides) in its bulk form, crystallizes in the cubic ZB phase. This phase is very similar to diamond structure [1] where the two sublattices at $(0; 0; 0)$ and $(1/4; 1/4; 1/4)a_c$ are occupied by Ga and As atoms, respectively, as shown in figure 1.4a.

In GaAs NWs, however, the crystal structure can adopt different atomic structures, the so called *polytypes*. For NWs grown along the [111]B direction, polytypes with same in-plane structure but different stacking sequences with respect to bulk are quite often observed. Several polytypisms have been observed in III-V semiconductor NWs, among them the cubic ZB, in figure 1.4a, the hexagonal WZ, in figure 1.4b and the 4H structure are particularly relevant.

The stacking is ABCABC for the ZB structure, ABAB for the WZ structure and ABCBABCB for the 4H structure. Each letter (A, B, C) corresponds to a bilayer of atoms, consisting of one layer with group III (Ga) and one with group V (As) atoms [21], as shown in figure 1.5.

Because NW growth proceeds in a layer-by-layer scheme, often *stacking faults* and

---

[1]Diamond structure can be visualized as a face centered cubic (fcc) lattice with lattice parameter a_c, together with a basis of two atoms at the coordinates $(0; 0; 0)$ and $(1/4; 1/4; 1/4)a_c$ in the cubic unit cell.
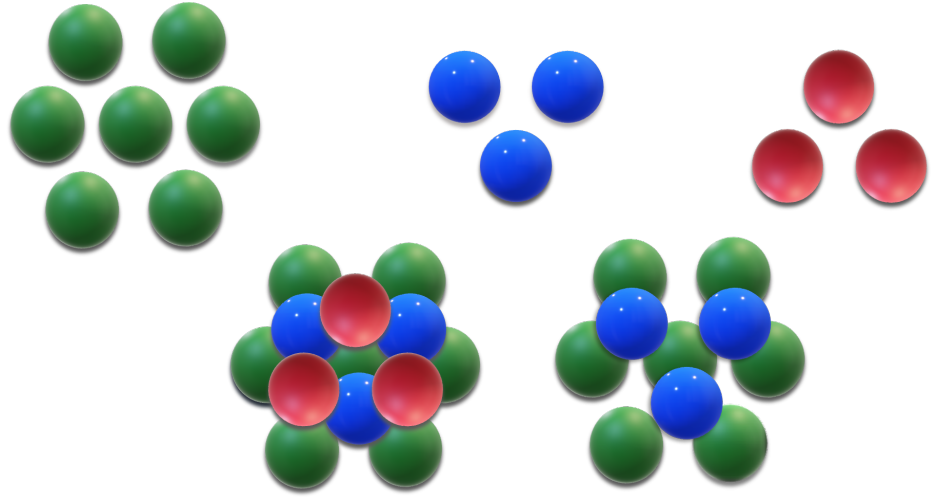
Figure 1.5: Top view of atomic closed packed layers (A, B and C) stacked along the [111] direction as ABC and AB.

rotational twins are observed. A rotational twin is a special type of stacking fault in the ZB lattice, by which the stacking sequence is inverted at a twin boundary, corresponding to a rotation of the initial ZB lattice by π along the growth direction. A rotational twin changes the initial sequence in the form (ABCAB|ACBA), with the twin boundary indicated by the vertical line [12].

1.3   Physics at the nanoscale

Due to the high aspect ratio of NWs, the surface to volume ratio acquires great importance, as well as the size and shape of the object. As the surface constitutes a break of the perfect crystal order, it is rich of defects, which originate electronic states within the band gap of the material. This modifies the band structure; which is directly related to the electronic properties of semiconductors. Furthermore, the band configuration is modified by the crystalline structure of the NWs, e.g because of the presence of polytypes and twin defects. It was observed, that the interface between different polytypes sections can affect the electronic and thermal transport [22].

The knowledge of the relation between structure and functionality is crucial to control and tailor physical properties, but it is very challenging to quantify the mentioned relationship. Furthermore, this usually requires the handling and measurement of single NWs. Some experimental techniques for electrical characterization of NWs will be described in the following chapter.

1.4 Applications of GaAs nanowires

Semiconductor NWs can be used in many possible fields [23]. In this paragraph, I will present an overview of some possible uses of these nanostructures. Semiconductor NWs can play a crucial role in:

- electronics: NWs can for example be used as active channel of FETs [24, 25, 26, 27];

- sensor device developement: NWs can be exploited as sensors for gaseous species [28] or as sensitive and selective chemical and biological sensors [29, 30];

- photonics: NWs can be used as flexible waveguides [31] or as lasers or LEDs [32, 33];

- photovoltaic applications [34, 35];

- fabrication of mechanical sensors and electromechanical devices based on piezo-electric semiconductor NWs [36].

A few examples for GaAs-based NW applications are listed below, in order to emphasise the need of tuning their structure and properties.

1.4.1 Electronic, photonic and optoelectronic applications

Transistors

Transistors are at the heart of many electronic device. The dimensions of NWs make them optimal candidates for the construction of very small transistors, allowing the dimensions of devices to scale as well. For example, Tomioka et al.[18] developed a high performance surrounding-gate vertical NWFET transistor using III–V materials. They are being explored as alternative fast channels on Si because of their high electron mobility and high-quality interface with gate dielectrics.

GaAs NW FETs have been demonstrated for detection of biological electrical activity, such as electrical activity produced by skeletal muscles and recorded as electromyogram [27].

Light Emitting Diodes

LEDs are semiconductor devices in which injected carriers recombine radiatively [37]. These devices consist in a forward-biased p-n junction: when a current flows through the device, the recombination rate will lead to an emission with energy corresponding to the semiconductor band-gap (E_g). Band-to-band recombination is the main mechanism that describes carrier activity within a LED. When an electron in the CB and a hole in the VB recombine, they lower their energy, that is released in the form of a photon. When the LED is forward biased, the bands bend slightly, decreasing the energy barrier
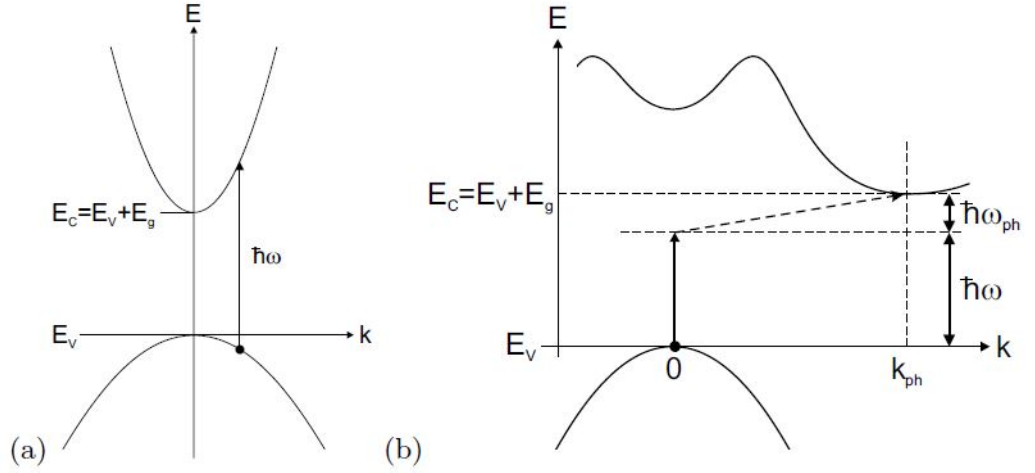
Figure 1.6: (a) Direct and (b) indirect optical transitions between VB and CB. The photon energy is E_g. The indirect transition involves a phonon with energy $\hbar\omega_{ph}$ and wavevector k_{ph} [37].

between the n- and p-type semiconductors. This reduced energy barrier enables more of the majority carriers to diffuse to the opposite side of the junction. Since the electrons from the n side become the minority carriers once they reach the p side, recombination is more likely to occur.

Direct band-gap materials are particularly convenient as LEDs materials, because they have a high probability of transition compared to indirect band gap materials (e.g. Si). The reason for this difference in recombination probability is clear from figure 1.6. In direct band gap semiconductors, the position of the top of VB and of the bottom of CB coincide in the reciprocal lattice, while in indirect band gap material this is no more true. In an indirect band structure the missing k difference (across the Brillouin zone) between VB and CB state needs to be provided by a phonon. But the two-particle process is less probable than the direct absorption that only involves the photon. Therefore, direct band gap materials are usually chosen to produce high efficient LEDs. It was observed (see e.g. [38]) that geometrical and structural properties of NWs strongly influence the performances of the devices.

Haraguchi [39] reports on the properties of GaAs nanowiskers, as LEDs, with intrinsic ultrasmall p-n junctions and the dependence of their infrared emission on the polarization, showing that the nanowhisker can be used as a quantum wire with a two dimensional quantum-confinement effect. The use of NWs as LEDs instead of bulk materials has many advantages, due to their optical and mechanical properties. In the work presented by Hahn and his group [33], they have shown the possibility of tuning color electroluminescence from blue to orange in $In_xGa_{1-x}As$ NWs with increasing In

composition. The possibility of tuning the color of emitted light allows to build tunable full-color LED arrays without the compromise between the device efficiency and light quality associated with conventional phosphor-based LEDs [40].

What is more, the high aspect ratio of NWs also allows to obtain flexible LEDs based upon inorganic materials. The production of flexible LEDs has a great economically relevance, for technological applications as rollable displays, wearable intelligent electronics and lightning. The use of inorganic semiconductors allows to overcome problems related to poor time stability and limitations in the short wavelength range presented by the OLEDs, traditionally used to achieve LEDs flexibility.

Nanolasers

The *laser* (Light Amplification by Stimulated Emission of Radiation) delivers intense, coherent electromagnetic waves [41]. The produced light beam is characterized by good temporal and spatial coherence and it is highly monochromatic. One of the major parts of laser structure, shown in figure 1.7, is the optical resonator (or resonating cavity), usually obtained using two mirrors, in which light can circulate. Within the cavity there is a gain medium, which serves to amplify the light. This gain medium requires some external supply of energy, i.e. it needs to be *pumped*, e.g. by injecting light (optical pumping) or an electric current (electrical pumping). The principle of laser amplification is stimulated emission. During light traveling between the mirrors, losses in intensity occur due to absorption, scattering, and reflections: in general, the laser will lase if, in a round trip the total gain obtained in the gain medium is higher than the total loss.

Semiconductor lasers are lasers based on semiconductor gain media, where optical gain is achieved by stimulated emission at an interband transition. Most of them are electrically pumped laser diodes, where electron-hole pairs are generated by an electrical current in a region where n-doped and p-doped semiconductor materials meet. However, there are also optically pumped semiconductor lasers, where the carrier generation is
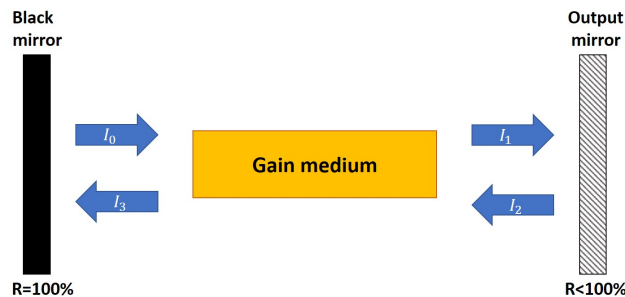

Figure 1.7: Structure of a laser: the light bunches between the two mirrors and it is amplified by the gain medium. The lasing condition is obtained whether $I_3 > I_0$.
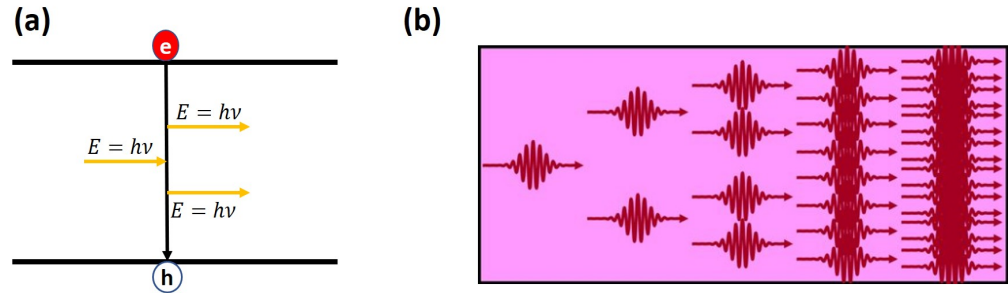
Figure 1.8: (a) Stimulated emission: an incoming photon triggers the transition of an electron in the CB into an empty state in the VB. The emitted photon is in phase with the initial photon. (b) Amplification in the gain media: if many molecules in a medium are excited, one photon can become many [42].

obtained by pumping light with energy close to the semiconductor band gap.

In a laser diode, light generation is obtained applying a forward bias to a p-n junction, causing current to flow. As the electrons from the n-type semiconductor flow into the p-type semiconductor, they combine with holes, releasing energy in the form of light. Optically pumped semiconductor lasers (OPSL) use a III-V semiconductor chip as the gain medium, and another laser (often another diode laser) as the pump source. Light amplification in the semiconductor medium is based upon stimulated emission, which amplifies the pumping signal. A nearby photon with energy equal to the recombination energy can cause recombination by stimulated emission. This generates another photon of the same frequency, polarization, and phase, traveling in the same direction as the first photon. This means that stimulated emission will cause gain in an optical wave (of the correct wavelength) in the injection region, and the gain increases as the number of electrons and holes injected across the junction increases. This gaining procedure and the stimulated emission process are schematized in figure 1.8.

NWs can be used as key element in lasers construction, simce they can act simultaneously as an optical gain medium and optical cavity that, in some cases, possesses the intrinsic capability to lase. This property, along with the ability to tune the emission wavelength and its potential for electrical integration with common materials as Si or Ge, makes the NW laser a promising candidate for use in the next generation of optoelectronic devices [43].

Since the first applications of ZnO NWs [44], other materials, such as nitrides and III-V semiconductors were successfully developed for laser applications. For example, Mayer et al. [45] reported on lasing in the infrared region with light emission from detached GaAs NWs at room temperature, where the GaAs active region was passivated with an AlGaAs shell, in order to inhibit the non-radiative surface recombination due to the high density of defects state at the surface.

Solar cells

A solar cell works through the absorption of light and the production of excitons, the separation of the charge carriers, and the external extraction of the separated carriers. The use of NWs-based building blocks for future solar energy conversion devices is an important matter of research for reasons of miniaturization and reduced material consumption, as well as for improved efficiencies [46]. In particular, the core-shell radial p-i-n structure is of particular interest, as it allows the light absorption and the carrier separation to be decoupled axially and radially, respectively, allowing to obtain the same efficiency with less material. It is predicted that such structures enable an extremely efficient carrier collection, as the minority carrier diffusion length can in all cases be shorter than the optical absorption length. This relaxes the demand for the material quality, which at the same time can lead to the reduction in the fabrication costs [47]. Colombo [47] published an example of p-i-n GaAs NWs growth on Si substrate for the production of solar cell devices. These has been recently characterized by Krogstrup [34], reporting an apparent efficiency up to 40%.

1.4.2 Piezo-electric applications

Piezo-electic materials can be used to harvest energy from mechanical vibrations[48]. Wang's group [36] demonstrated the principle of charge generation from the bending of piezoelectric ZnO NWs. This is possible due to the combination of the semiconducting and piezoelectric nature of ZnO. In group III-V semiconductors, the inverse piezoelectric effect arises from the lack of centro-symmetry along the [111] direction in the ZB and [0001] WZ crystal structures.

Remarkable differences have been observed in comparison to bulk materials. Minary-Jolandan and his group [49] determined the piezo-electric coefficients of single GaN NWs, showing an increase of up to six time the effect known from bulk.

1.4.3 Electrical and optical properties

ZB GaAs is a direct band gap semiconductor with a band gap of E_g =1.425 eV at room temperature. An agreement on WZ GaAs band gap has not been reached so far, because of the strong dependence of the values extracted on the experimental parameters, but previous studies determined the band gap to be between 20 meV and 55 meV below the gap of ZB GaAs [50].

From an electrical point of view, the high aspect ratio of the NWs compared to bulk has a strong impact on the electrical parameters. The surface is a source of surface states, which are localized within the band gap and are responsible for a pinning of the Fermi level. The effect of surface states was studied by Casadei et al. [51]: they underlined the

importance of surface passivation on highly doped GaAs NWs, in order to increase the value of the effective mobility of the charge carriers.

From an optical point of view, from photoluminescence studies performed by Hoang et al. the direction of linear polarization of the emitted light was determined: it was mainly perpendicular to the growth axis for WZ and parallel to the growth axis for ZB [52]. A staggered-type II band alignment has also been observed [51] [52] at the ZB/WZ heterointerfaces, as schematized in figure 1.9. That means that the minimum energy of the conduction band and the maximum of the valence band are located in the two different polytypes, implying a longer recombination time and a reduced exciton binding energy.
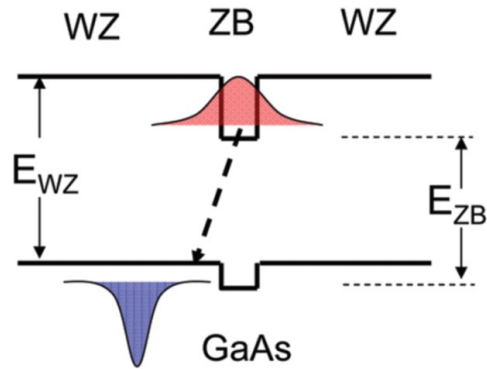

Figure 1.9: Schematic diagrams of the band alignment and recombination processes for WZ GaAs NW with a nanometer thin ZB GaAs segment created by stacking faults [52].

Chapter 2

Electrical characterization of nanowires

Chapter 2 presents an overview on some possible methods for electrical characterization of NWs. It also includes the theoretical part concerning the metal-semiconductor interface, to describe the contact between the semiconducting NW and the metallic probe used for characterization.

2.1 Experimental methods for electrical characterization of nanowires

2.1.1 Traditional approach: Field Effect Transistor configuration

As highlighted in section 1.4 semiconductor NWs have been studied extensively for their novel electronic, photonic, thermal, electrochemical and mechanical properties [23, 53]. Applications in these fields often make use of single NWs [34, 18, 32], whose properties are strongly influenced by structural parameters such as phase purity or lattice strain [54]. For the development of future NW applications, therefore, it is crucial to study how the resistivity and exact I-V properties of single NWs determine the performance of the entire device.

Electrical transport in semiconductor NWs is commonly measured in a FET configuration [55, 56]: here, the NW to be characterized is removed from its original growth substrate and laterally deposited onto an insulating substrate. Then, the NW is contacted with 2 or 4 metallic electrodes, usually deposited via FIB or via EBL, as shown in figure 2.1. Then, by applying tension between the source and the drain, the current passing through the NW is measured and the I-V characteristic is acquired.

However, this approach is labor intensive, requires high-end fabrication equipment, exposes the NWs to extensive processing steps, provides channel rather than bulk mobility, can be strongly affected by surface and interface states and places practical limitations on minimum NW length [58]. What is more, recent technological applications
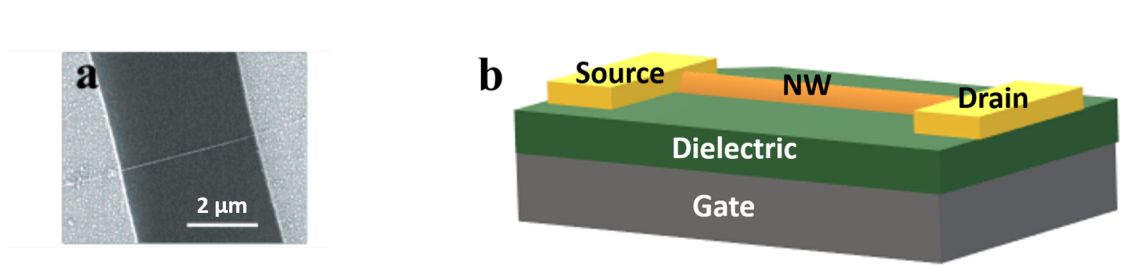
Figure 2.1: (a) FE-SEM image of a GaN NW FET [57] and (b) Schematic of a NW FET.

demand the use of NWs in their as-grown geometry on the substrate, while the fabrication of NW FET structures comprises the transfer of the NW on an insulating substrate. This can significantly alter electric transport properties of the NW: the properties of NW-FET configuration can be substantially different from the properties of as-grown NWs [59, 60, 61]. For these reasons, a series of alternative characterization techniques have been developed for electronic characterization of as-grown NWs on their growth substrate.

2.1.2   Characterization of as-grown nanowires

One of the alternative techniques for the characterization of single free standing NWs on their growth substrate involves the use of sharp metallic probes with precise position control to acquire the I-V characteristic of NWs. This measurement can be obtained either in a 2-terminal or in a 4-terminal configuration. The STM has been proved to be a suitable tool for directly measuring the I-V characteristic of single NWs. An integrated SEM system can be used to visualize the NWs and the approaching tips.

In the 2-point probe configuration, the two metallic needles contact respectively the top of the NW (or its side wall) and the substrate, as shown in figure 2.2. The tip placed on the top of NW is used to inject and to measure the electrical current I through the NW, the substrate is used as contact to close the circuit. This configuration presents two important limitations for the electrical measurements and for the comparison of characteristics of different NWs. The first one is due to spurious resistances: beside the NW resistance, the measurement also includes the substrate resistance and the contact resistances. While the first parameter is usually negligible, being the substrate highly doped with respect to the wire, the latter should be considered, especially when one wants to characterize doped NWs. The second problem is due to the random nature of the contact area between the single NW and the substrate. Using the experimental setup described above, it is impossible to measure the contact area between NWs and the substrate, and this parameter is different from NW to NW. Since it is supposed to influence the resistance of free standing NWs, the comparison between resistances of
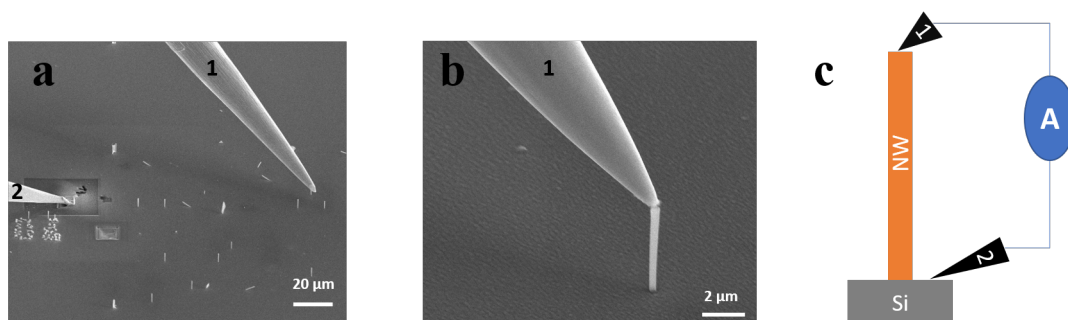
Figure 2.2: (a)SEM image of W-tips contacting a NW and (b) Zoom on the contact Schematic of contacting NW.
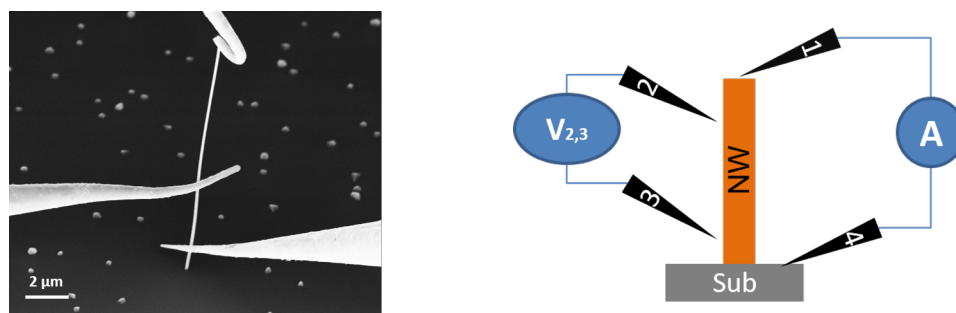
Figure 2.3: (a)SEM image of three W-tip contacting a NW. The second contact is on a Pt layer, deposited on the substrate to increase the current signal, (b)zoom of the probe contacting the top of the NW and (c)schematic of contacting NW.

different wires requires the use of a measurement independent of the contact area.

In the 4-point probe configuration, other two tips are added along the side walls of the wire for potential measurements, as shown in figure 2.3. By using this setup, the contact resistance of tips 2 and 3 can be neglected. This technique allows to overcome the limitations of the 2-terminal measurements, but it is much more challenging to be obtained experimentally, and there is a limited literature on the use of this method.

Both configurations also allow to measure the resistance profile along single NWs. In the 2-terminal geometry, this measurement can be performed by moving the tip along the side wall of the wire, and repeating the I-V characterization point by point. In the 4-terminal geometry, two tips are kept fixed on the wire (as well as the one contacting the substrate) while the remaining one is moved along the side wall of the NW, measuring resistance profiles with higher spatial accuracy [46].

2.2   Theoretical models

2.2.1   Multiple regimes in a nanowire characteristic

As illustrated above, one of the most popular approaches for electrical characterization of semiconductor NWs is to probe them with a metallic needle, generating a MS contact. In the 2-terminal configuration, the influence of the contacts on the measured resistance cannot be avoided, and should be taken into account in data analysis.

A MS contact can assume a rectifying behaviour (Schottky contact) due to a potential barrier induced by spatial charges in the semiconductor; or can assume a metallic (ohmic) behaviour with a resistance independent on the applied voltage [62]. The metal and the semiconductor have generally different positions of the Fermi levels relative to the vacuum level. When the metal is in contact with the semiconductor, charges will flow in such a way that in thermodynamic equilibrium the Fermi level is constant throughout the structure [37]. The theory on current injection in solids can be easily described by considering the simplified model of one-carrier currents, hence neglecting the minority carrier contribution. In particular, for simplicity of description, from now on, only the case of n-type semiconductors will be considered. The injection level (i.e. the applied voltage) determines the presence of different regimes, which can be treated by assuming a constant mobility and negligible diffusion of the charge carriers, and free and trapped carriers in quasi-thermal equilibrium (which implies a change in the Fermi level value) [63].

According to A. Cavallini and L. Polenta [63], current-voltage characteristics are classified depending on the type of contact, which will be described below.

I-V characteristics with Ohmic contacts

A typical characteristic of a n-type semiconductor may contain up to four different regimes, depending on the injection level: regime of ohmic conduction, Space Charge Limited Conduction (SCLC), Trap Filled Limited Conduction (TFLC) and Trap-free Space Charge Limited Conduction.

1. Ohmic conduction regime: the current is dominated by thermal electrons, present in higher concentration with respect of injected ones. In this regime the free carrier concentration is independent on the applied voltage and Ohm's law is valid: the current density is then given by equation 2.1, where σ is the conductivity of the material and E is the applied electric field (spatially constant in this regime).

$$J_{\text{Ohm}} = \sigma E \tag{2.1}$$

2. SCLC regime: this regime occurs when the number of injected carriers exceeds the number of thermal carriers. In a trap-free material, by neglecting the diffusion
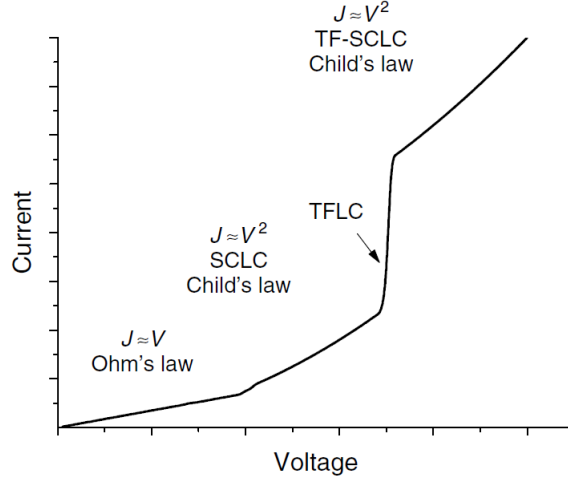
Figure 2.4: Current–voltage behavior with injecting contacts [63].

current and the dependence of the carriers mobility μ on the electric field, the concentration of the free carriers depends on the applied voltage and the current density depends on the square of the applied voltage. From Mott-Gurney's law [64]:

$$J_{\text{Mott-Gurney}} = \frac{9\epsilon\mu V^2}{8L^3} \tag{2.2}$$

where ϵ and L are the dielectric constant and thickness of the material respectively, μ is the mobility of the charge carriers, and V is the applied voltage.

3. TFLC regime: the space charge is dominated by trapped electrons but the current is carried by the injected free electrons, whose number is not a constant fraction of trapped electrons.

   Empty traps become scarce: the injected trapped carriers are still dominant but the number of injected free electrons rapidly rises, and so does the current. This regime is usually characterized by a fixed voltage corresponding to the space charge of the injected trapped electrons, whose value depends on the square of the layer thickness.

4. By further increasing the bias, hence the injection level, injected free electrons exceed the injected trapped electrons and dominate the space charge. Again the number of free carriers is proportional to the space charge and the SCL current flows. Hence, in this regime, the dependence of current on the square voltage is valid again.

The current-voltage behaviour in the different regimes is plotted in figure 2.4
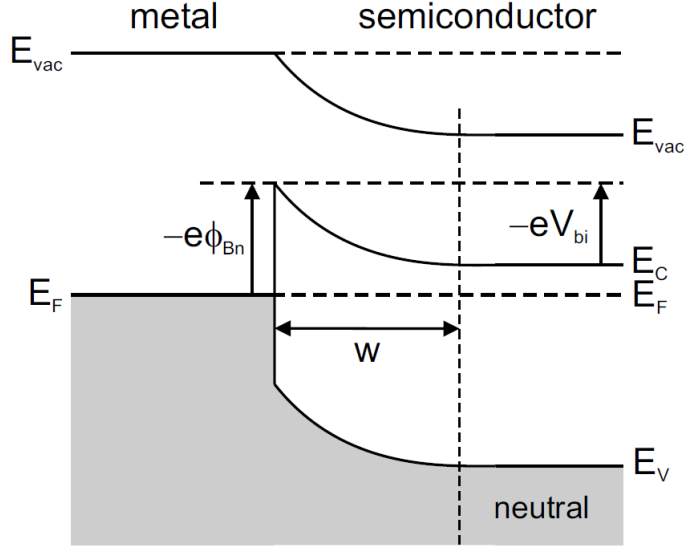
Figure 2.5: Schematic band structure of a metal–semiconductor junction that is dominated by bulk properties of the semiconductor: w denotes the width of the depletion layer, $\phi_{B,n}$ denotes the Schottky barrier height, V_{bi} denotes the built-in voltage [37].

I-V characteristics with Schottky contact: thermionic emission

The intimate contact between the metal and the (n-type) semiconductor, neglecting surface states or oxide interfaces, gives rise to a band bending: free electrons move across the interface to align Fermi levels to satisfy the thermodynamic equilibrium. This leads to the creation of an electric field and therefore of a depletion layer, where uncompensated positive donors lie. The situation is schematized in figure 2.5.

In thermal equilibrium, the band bending originates a potential barrier (Schottky barrier), ϕ_B opposed to the flow of electrons from metal to semiconductor. The height of the barrier is given by equation 2.3 for an n-type semiconductor and by 2.4 for a p-type semiconductor:

$$\phi_{B,n} = \phi_M - \chi_S \tag{2.3}$$

$$\phi_{B,p} = -\frac{E_G}{e} + \phi_M - \chi_S \tag{2.4}$$

where e is the elementary charge, ϕ_M is the work function of the metal, and χ is the electron affinity of the semiconductor.

When an external bias V is applied, the Fermi level of the semiconductor is shifted up (forward bias) or down (reverse bias) changing the charge flux between the two materials. At thermal equilibrium the net carrier density is null, as the two flows of carriers are opposite. The current flowing through the contacts is mainly due to the motion of the

majority charge carriers: at room temperature for slightly doped semiconductors the dominating transport mechanism is the thermoelectric emission of the majority charge carriers which pass the potential barrier. The current density of negative charges from the semiconductor to the metal is [65]:

$$J_{S \to M} = \frac{pen\mathbf{v}}{4} = \frac{peN_C\mathbf{v}}{4}exp(\frac{e(\phi_{B,n} - V)}{k_BT})$$ (2.5)

where p is the tunneling probability of the electrons through an hypothetical thin insulating layer at the interface, T is the temperature, ϕ_B is the height of the Schottky barrier, k_B is the Boltzmann constant, e is the elementary charge, V is the voltage applied to the contact, n is the electron concentration in the semiconductor[1]. Assuming an isotropic distribution of velocities, according to Maxwell distribution, $\frac{n\mathbf{v}}{4}$ is the number of incident electrons (per area unit and per second) on the insulating layer, with $\mathbf{v} = \frac{8k_BT}{\pi m_{eff}}$ average thermal velocity of the electrons, being m_{eff} the effective mass of electrons in the semiconductor.

If the bias is changed, the current from the semiconductor to the metal increases in the forward direction because the energy difference between the quasi-Fermi level and the top of the barrier is reduced and is reduced for reverse bias. The barrier from the metal into the semiconductor remains constant: hence, the current from the metal into the semiconductor is independent on the applied bias [37]. The current flowing from the metal into semiconductor can can be obtained from the condition $J = 0$ for zero bias, and is given by:

$$J_{M \to S} = \frac{pen\mathbf{v}}{4} = \frac{peN_C\mathbf{v}}{4}exp(\frac{e\phi_{B,n}}{k_BT})$$ (2.6)

The resulting current, $J = J_{S \to M} - J_{M \to S}$ can be rewritten as:

$$J = A^*T^2exp(\frac{e\phi_{B,n}}{k_BT})(exp(\frac{-eV}{k_BT}) - 1)$$ (2.7)

where The Richardson constant is given by:

$$A^* = \frac{4\pi em_{eff}k_B^2}{h^3}$$ (2.8)

with $p = 1$ for an infinitely thin insulating layer and $N_C = 2(2\frac{\pi m_{eff}k_BT}{h^2})^{3/2}$, being h the Planck constant.

As shown from the equations above, at the thermodynamic equilibrium two opposite equal fluxes of charge carriers result in no current. When a voltage is applied to the contact, the barrier height changes and the resulting current is not zero any more. In

---

[1]$n = N_Cexp(\frac{e(\phi_{B,n} - V)}{k_BT})$, where N_C is the effective density of states.

particular, the barrier is reduced in case of forward bias and is increased in the case of inverse polarization.

In the ideal model describing Schottky contacts the height of the barrier ϕ_B is overestimated [37]. In real Schottky contacts, the presence of surface states of the semiconductor at the interface influences the barrier height, which results almost independent on the work function of the metal. Other lowering factors may be the Schottky effect (image-charge effect), the existence of an insulating layer at the interface between the NW and the metallic probe [66], and the field penetration [65]. An I-V characteristic for a generic Schottky junction in thermoelectric condition can be expressed as:

$$J = A^* T^2 exp(\frac{e\phi_{B,n}}{k_B T}) exp(\frac{-eV}{k_B T n_{ideality}})$$ (2.9)

when $V > \frac{3k_B T}{e}$, where $n_{ideality}$ is the ideality factor of the diode (1 in the ideal case).

In real diodes a series resistance has usually to be taken into account, and equation 2.9 becomes:

$$J = A^* T^2 exp(\frac{e\phi_{B,n}}{kT}) exp(\frac{-e(V - R_s I)}{k_B T n_{ideality}})$$ (2.10)

According to the method presented by Cheung and Cheung [67], it is possible to extract the resistance R_s in series with the Schottky diode in equation 2.10 using:

$$\frac{dV}{d(lnJ)} = R_s A_{eff} J + \frac{n_{ideality}}{\frac{e}{k_B T}}$$ (2.11)

where A_{eff} is the cross section of the contact.

Tunneling current: Field Emission and thermionic Field Emission

At high doping or low temperature conditions, thermionic emission is no longer the dominant mechanism, since tunneling through the barrier becomes relevant. In particular, in high doping conditions, the width of the depletion layer, given by equation 2.12, becomes smaller and tunneling processes become more probable [37].

$$w = \sqrt{\frac{2\epsilon_s}{eN_d}(V_{bi} - V - \frac{k_B T}{e})}$$ (2.12)

where V_{bi} is the built-in voltage and N_d the net concentration of donor levels.

Two processes are important in describing tunneling current. The first one, that is of particularly importance in case of degenerate semiconductors at low temperature, is the Field Emission (FE) and corresponds to the tunneling of electrons close to the Fermi level of the semiconductor. The second one, the Thermionic Field Emission (TFE), becomes relevant when the temperature is raised: electrons are excited to higher energies where they encounter a thinner barrier, and tunneling probability increases.

Chapter 3

Experimental techniques and numerical simulations

Chapter 3 presents an overview on some experimental techniques which are suitable for NW growth and characterization. In particular, it describes MBE for NW growth and SEM and STM for the sample visualization and morphological characterization. It also presents the FIB technique, that is suitable for both the characterization and the patterning of a given structure.

Finally, after the experimental section, this chapter also includes one section about FEM simulations, a numerical method for solving continuous problems of engineering and mathematical physics.

3.1 Molecular Beam Epitaxy

Epitaxy in general means the deposition of a crystalline layer on another crystal (the substrate), maintaining the crystalline order. Some of the most promising techniques for epitaxial growth are for example MBE, CVD and LPE. In particular, MBE is a suitable and versatile technique for growing thin epitaxial structures made of semiconductors, metals or insulators. This technique is usually an atomic layer by layer crystal growth technique, based on reaction of molecular or atomic beams with a heated crystalline substrate, performed in an UHV environment (pressure is around $10^{-8} - 10^{-9} Pa$).

The MBE technique allows to obtain clean, atomic level controlled surfaces to be used as an epistratum for device fabrication. Structures grown through MBE are characterized by high purity and crystal quality, low defect density, controlled doping profiles and high repeatability and uniformity. These qualities are ensured by a very precise control of the beam fluxes and growth conditions. The high crystal quality is assured by the small amount of impurities in the system and a low growth rate that allows surface migration, resulting in smooth surfaces. Moreover, being realized in an UHV environment, the
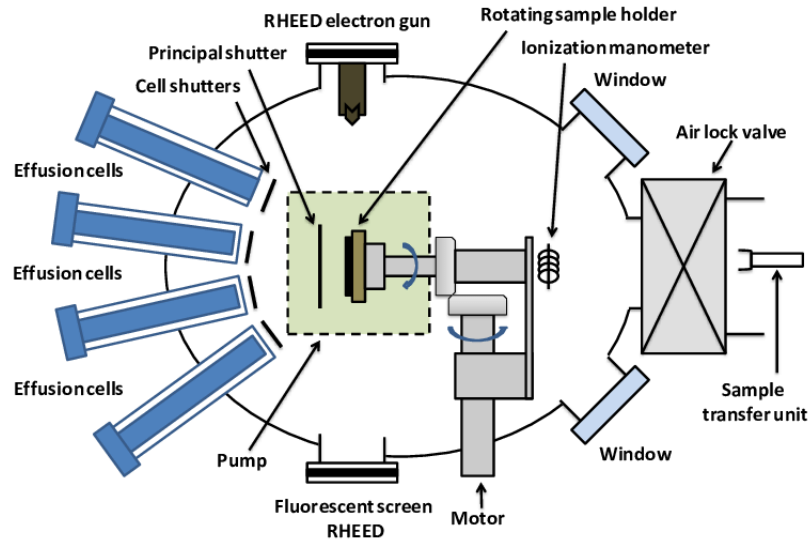
Figure 3.1: Schematic of principal elements of MBE system [69].

growth may be controlled in situ by surface diagnostic methods such as Reflection High-Energy Electron Diffraction (RHEED) [68].

3.1.1 MBE setup

A schematic of a MBE system is shown in figure 3.1. The region on the left side of the schematic is the generation zone of the molecular beams, where these are generated from sources of the Knudsen (effusion) cell type. The temperature of effusion cells is precisely controlled, to control the flux stability. By choosing appropriate cell and substrate temperatures, epitaxial films of the desired chemical composition can be obtained.

Next, in the center of the image, is the zone where the beams from different sources intersect each other and the vaporized elements mix. The presence of a RHEED system allows to control *in situ* the growth of the structure. The gas mixture finally contacts the substrate area, whose temperature is precisely controlled, to ensure the formation of a very high quality structure.

3.1.2 MBE growth mechanisms

In MBE, the important processes for the crystal growth take place directly at the substrate surface: the growth is mainly determined by the kinetics of the involved surface processes. The most important processes [68] are:

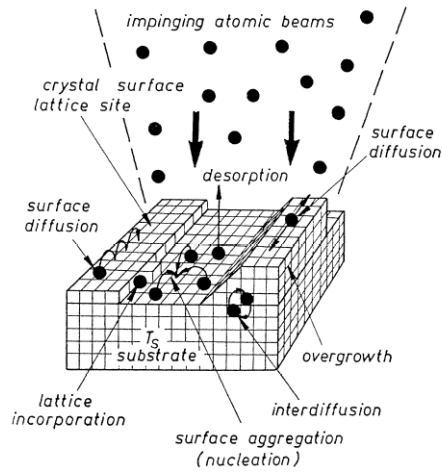1. adsorption of supplied molecules or atoms on the substrate surface

Figure 3.2: Different processes that are involved in the growth by MBE [68].

2. surface migration and dissociation of molecules

3. incorporation of atoms into the crystal lattice

4. thermal desorption of the not incorporated atoms

These processes are schematically illustrated in figure 3.2. The substrate crystal surface is divided there into crystal sites (created by dangling bonds, vacancies, step edges...) with which the impinging molecules or atoms may interact. The adsorbed molecules (or atoms) first combine to reach a critical size and then become stable nuclei (or clusters) on the substrate. The main factors affecting the critical size are the substrate temperature, the arrival rates and the affinity with the substrate. Subsequent molecules (or atoms) may condense directly onto these nuclei, decreasing the rate of formation of new nuclei and increasing the size of existing ones.

Depending on the interaction strength between adatoms and the surface, three possible modes of crystal growth on surfaces may be distinguished, as shown in figure 3.3.

In the island, or *Volmer-Weber* mode, small clusters are nucleated directly on the substrate surface and then grow into islands of the condensed phase. This happens when the deposited atoms (or molecules) are more strongly bound to each other than to the substrate. This mode is the most commonly displayed by systems of metals growing on insulators.

The layer-by-layer, or *Frank-van der Merwe* mode, is displayed by atoms (or molecules) that are more strongly bound to the substrate than to each other. In this mode, the
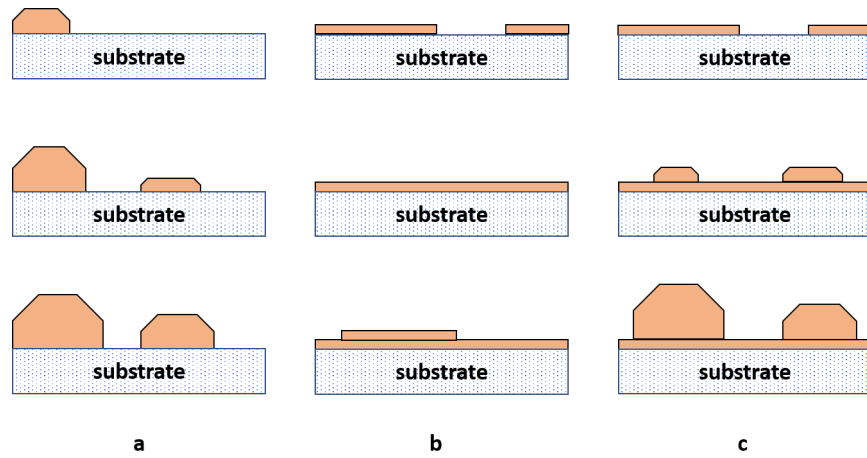
Figure 3.3: Schematic representation of the three crystal growth modes. (a)Frank-van der Merwe mode (b)Volmer-Weber mode (c)Stranski-Krastanov mode.

first atoms to condense form a complete monolayer on the surface, which becomes covered with a second layer and so on. This growth mode is often observed in the case of adsorbed gases, such as several rare gases on graphite and on several metals, in some metal-metal systems, and in semiconductor growth on semiconductors.

The layer plus island, or *Stranski-Krastanov* mode, is an intermediate case. After forming the first monolayer, or a few monolayers, subsequent layer growth is unfavorable and islands are formed on top of this intermediate layer. Transition from the layer-by-layer to island-based growth occurs at a critical layer thickness which is highly dependent on the chemical and physical properties, such as surface energies and lattice parameters of both the substrate and film.

3.2 Scanning Electron Microscopy

The SM is an instrument that allows the creation of magnified images and the analysis of both bulk specimens and nanostructures. It allows to reveal microscopic-scale information on the morphology, composition, crystallography, and other physical and chemical properties of the sample. SEM allows to reach a spatial resolution of few nanometers.

A schematic diagram of an electron optical column for a two lens SEM is given in figure 3.4a. The basic operating principle of the SEM involves the creation of a finely focused beam of energetic electrons, emitted from an electron source, typically over a voltage range from 0.1 to 30 keV. The microscope is a probe forming system where each lens condenses and demagnifies the electron source to a focused spot at the specimen surface. The image is created by collecting outgoing electrons produced by the interactions between the sample and the primary electron beam. To minimize the
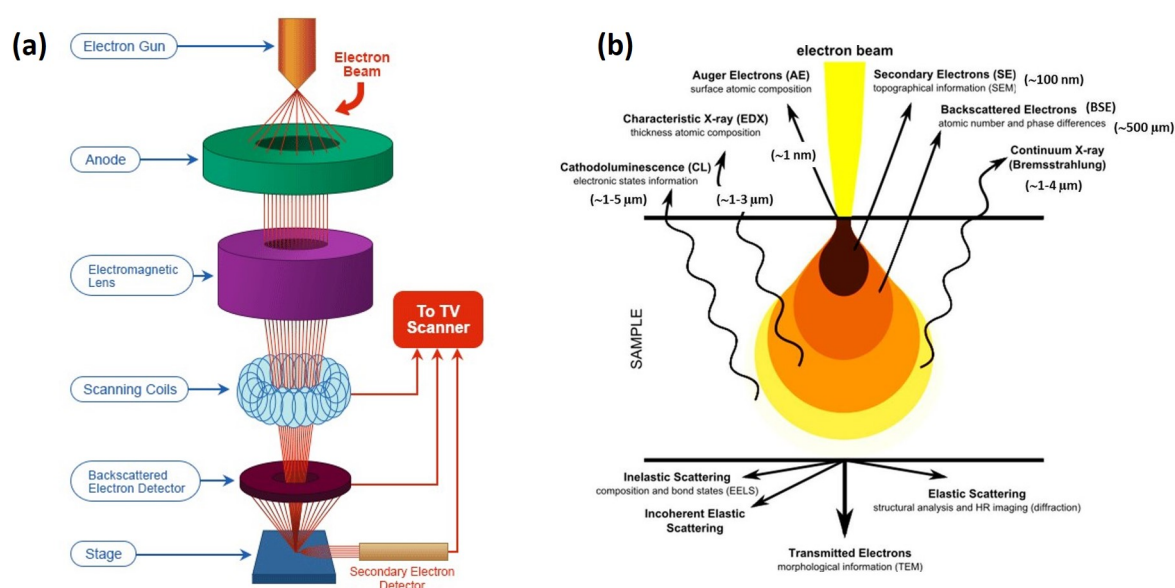
Figure 3.4: (a) Schematics of a SEM [70] and (b) Signals emitted from different parts of the interaction volume [71].

unwanted scattering that beam electrons as well as the outgoing electrons would suffer by encountering atoms and molecules of atmospheric gasses, the whole system is kept under vacuum conditions ($< 10^{-3} Pa$) [41].

After emission from the source and acceleration to high energy, the electron beam is modified by apertures, magnetic and/or electrostatic lenses, and electromagnetic coils. These objects are used to successively reduce the beam diameter and to scan the focused beam in a raster (x-y) pattern to place it sequentially at a series of closely spaced but discrete locations on the specimen. This procedure allows to obtain a topographic map of the sample: the SEM image is formed by the different signals produced when the electron beam interacts with the bulk specimen, at each discrete position analysed during the scanning procedure [72]. The energy spectrum of interaction products consists of contributions from secondary electrons (SEs), backscattered electrons (BSEs), Auger electrons (AEs) and X-Rays. As shown in figure 3.4b, each different signal provides different information [73].

3.2.1 Imaging Modes of Scanning Electron Microscopy

Secondary Electrons

SEs are emitted by specimen atoms ionized by primary electrons, and provide information about surface structure and local electric and magnetic fields.

In the SE operating mode, electrons can be collected easily by means of a positively biased collector grid placed on one side of the specimen. SEs usually have a low energy (2-5 eV), thus they can only escape from a region within a few nanometers of the material surface. SE signal provides information about surface texture and roughness with resolution down to 1-10 nm. Topographic contrast arises because secondary electrons generation depends on the angle of incidence between the beam and sample. SEs are retarded by a positive bias and repelled by a negative bias of the specimen and are influenced by the electrostatic field between regions at different biases. Thanks to these effects, a voltage contrast is generated: negatively biased areas appear bright and positively biased regions, dark. Due to the low exit energy, the SE trajectories are also affected by the magnetic stray fields of ferromagnetic domains, providing also information about local magnetic fields.

Backscattered Electrons

BSEs are the product of elastic collisions between electrons and the specimen atomic nucleus, that cause primary electrons to bounce back with wide-angle directional change. They provide information about surface structure and average elemental composition.

BSEs usually have energy higher than 50 eV. Unlike SEs, BSEs move on straight trajectories and are not affected by electrostatic collection fields: the detectors have to be mounted with a large solid angle of collection. Since the BSE emission also depends on the surface tilt, the surface topography can be imaged at lower magnifications with a better shadow effect than with SEs, owing to the straight trajectories and at higher magnification with a worse resolution, due to the larger information volume and exit area.

The most important contrast mechanism with BSEs is the dependence of the backscattering yield on the mean atomic number Z, which allows phases with different values of Z to be recognized: high average Z appear brighter than those of low average Z.

X-Rays and Auger Electrons

X-rays and AEs are created by the collision between primary electrons and inner shell electrons of the specimen atoms. When an inner shell electron is excited by collision with a primary electron, an outer shell electron will fall into the inner shell to return the atom to ground state. This can occur either by the emission of an x-ray photon or by the emission of an AE.

X-Rays and AEs provide information about elemental composition with different thickness-sensitivity.

At each beam location, outgoing electron signals are measured using electron detectors. The signal measured at each individual raster scan location on the sample is digitized and recorded into computer memory, and used to determine the gray level at
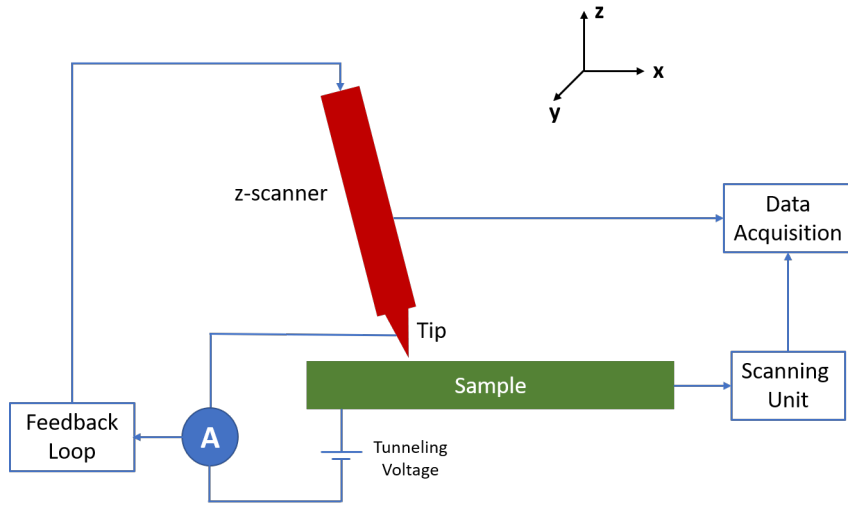
Figure 3.5: Schematics of a STM.

the corresponding X-Y location of a computer display screen, forming a single pixel of the image.

3.3 Scanning Tunneling Microscope

The general principle of scanning probe microscopes is to move a sharp tip close to a surface in order to measure various properties with a spatial resolution on the nanometer or even atomic scale. The STM was the first tool for scanning probe microscopy, invented in 1981/1982 by Binnig and Rohrer [74]. One of the most striking property of this kind of microscope is the possible resolution down to 1 Å in real space, that allows to readily resolve individual atoms. Moreover, it is capable of giving information on the distribution of single atoms on a conducting surface.

A schematic of STM, with fine metallic tip (usually made of W or Pt-Ir alloy) used as a probe, is shown in figure 3.5.

3.3.1 Working Principle

The tip is approached toward the sample, until the separation between the two is just a fraction of a nanometer. The electron wavefunctions in the tip overlap with the electron wavefunctions in the sample surface, generating a finite tunneling conductance: by applying a bias voltage between the tip and the sample, a tunneling current arises [75]. This tunneling current increases exponentially with decreasing tip-sample distance: by measuring the current flowing it is possible to measure (and control) the tip-sample distance very precisely. The tip is positioned and controlled with high accuracy, allowing

such a small resolution, using piezoelectric actuator elements.

The STM operates by bringing the tip close to the surface at a distance smaller than 1 nm, to obtain a given current I. The tip or the specimen is then slowly rastered in the x and y directions. While the tip is moving along the surface in x y direction, a feedback loop constantly adjusts the height of the tip to maintain constant the tunneling current, thereby providing the surface topography of the specimen by measuring variations in z direction [76]. The design of the instrument has to accommodate vibrations, temperature changes and the position of the tip. The STM is ideally suited to the study of surfaces in UHV. We can obtain good results even by using AFM, a device based upon the same principles working at atmospheric pressure, because the number of gas atoms in the space between the tip and the surface is not sufficient to significantly affect the tunnelling of electrons [41].

3.4   Focused Ion Beam

A FIB instrument is a powerful tool for analysis, selective deposition and sputtering of materials. The FIB technique is based upon a focused-ion beam directed towards the target material causing its sputtering. The FIB is commonly used for the preparation of specific samples and for imaging with secondary electrons produced by the ion beam. FIB can be either used in a single FIB chamber or combined with an SEM: a FIB/SEM chamber includes both a FIB column for sample preparation and an SEM column for observing the sample during preparation and for post-preparation analysis, using all of the imaging modalities and analytical tools available on a standard SEM column.

3.4.1   Instrumentation

FIB instruments are very similar to SEMs, but rather than using a beam of electrons FIB systems use a finely focused beam of ions that can be operated at low beam currents for imaging or at high beam currents for site specific sputtering or milling. FIBs can also be used to deposit material via ion beam induced deposition.

A FIB system, as shown in the scheme in figure 3.6a is composed by a vacuum system and chamber, a liquid metal ion source, an ion column, a sample stage, detectors and a gas delivery system. The majority of the FIB tools use either a liquid metal ion sources (LMIS) or a plasma source to produce ion beams with variable current. Once the ions are extracted from the source, they are accelerated through a potential (typically 5-50 eV) down the ion column. This latter usually has two lenses: a condenser lens and an objective lens. Lenses used for FIB systems are electrostatic lenses (unlike the magnetic ones used in SEM systems), that require high voltages to focus energetic ions due to their relatively large mass to charge ratio.

In order to understand the possibilities offered by the FIB technique, it is important to
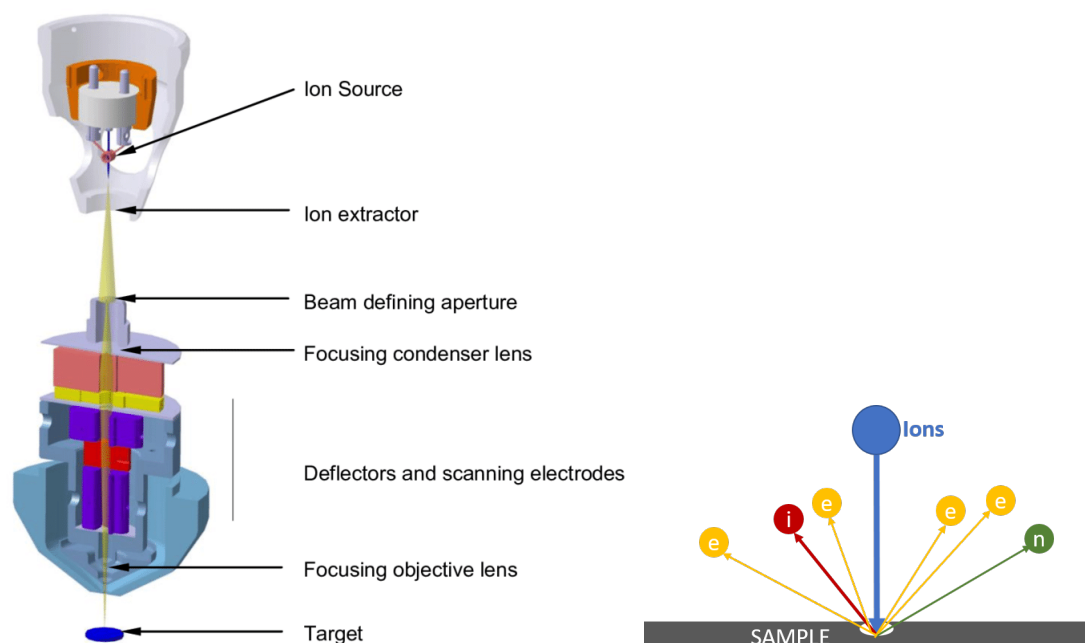
(a) Schematics of a FIB chamber [77].

(b) Schematic of ion/sample interaction.

know the interactions that can take place between the sample and the incoming ions. As shown in the scheme 3.6b, the primary ion beam, by hitting the sample surface, sputters a small amount of material and produces a beam of secondary electrons (ion induced secondary electrons). The sputtered material leaves the surface as either secondary ions i or neutral atoms n. Therefore, FIB can be used to remove material via sputtering, to deposit materials via ion induced deposition and for imaging, using secondary electrons.

3.4.2 Ion sputtering

FIBs can be used for direct and maskless patterning of a substrate. When the ion beam hits the substrate, incident ions transfer momentum to the material and release atoms through cascades of collisions. Practically any material can be sputtered and also visualized by FIB of 5-10 nm spot size. The main advantages of FIBs are the fast material removal rate compared to chemical etching and the small spot size, which is useful for microfabrication with submicrometer accuracy.

Layers of selected size can be removed from the substrate by rasterizing the surface with the ion beam. During line by line scanning, the ion beam pauses on each point for a certain time. Since FIB sputtering can be utilized for material removal, it is a feasible and efficient process for many areas of microengineering field, e.g. for the fabrication of micromilling tools, sharp AFM tips, nanopillars and nanopores [78].

3.4.3   Material deposition

FIB tools are often equipped with gas-injection systems (GIS) that can be used during sample preparation to deposit controlled layers of different materials. Common precursor gasses used can deposit for example tungsten, platinum, or carbon. The precursor gasses are deliverd to the sample surface through a small needle that is placed in very close proximity to the area of interest. The molecular gas deposited on the surface is then decomposed by the ion beam [79].

3.4.4   Imaging

At low beam currents, FIBs can be used to perform imaging topography of the studied sample. The ion induced secondary electrons (iSEs) signal can be collected and imaged just like secondary electrons produced with an electron beam and analyzed using SEM. FIB columns are all equipped with one or more iSE detectors.

iSE imaging has some advantages over SE imaging in the SEM. First, the ion beam produces many more SEs per incident particle than does a similar current electron beam resulting in a high signal, low noise image. Also, the iSE signal collected in a FIB is free of the BSE component that reduces contrast in SEM images. Moreover, iSE images show intense grain orientation contrast, allowing to image grain morphology without needing chemical etching. FIB secondary ion images also reveal chemical differences, and are especially useful in corrosion studies, since secondary ion yields of metals can increase by three orders of magnitude in the presence of oxygen, clearly revealing the presence of corrosion [80].

3.4.5   SEM/FIB dual-beam systems

A *dual-beam* instrument combines a SEM with a FIB, as shown in figure 3.7. This combination allows to provide simultaneously in situ specimen modification through precision ion beam sputtering and/or ion beam mediated material deposition and almost instantaneous image of the results in a non-destructive manner with the electron probe.

3.5   Finite Element Method

The description of the laws of physics for space- and time-dependent problems are usually expressed in terms of *partial differential equations* (PDEs). Some physical phenomena may be modeled using a finite number of defined components: we can refer to these type of systems as *discrete*. On the other hand, many physical systems, the so called *continuous* systems, can only be defined by a subdivision which continues indefinitely. In this case, the problem can only be solved using the mathematical fiction of an infinitesimal, leading to differential equations which imply an infinite number of elements. Using
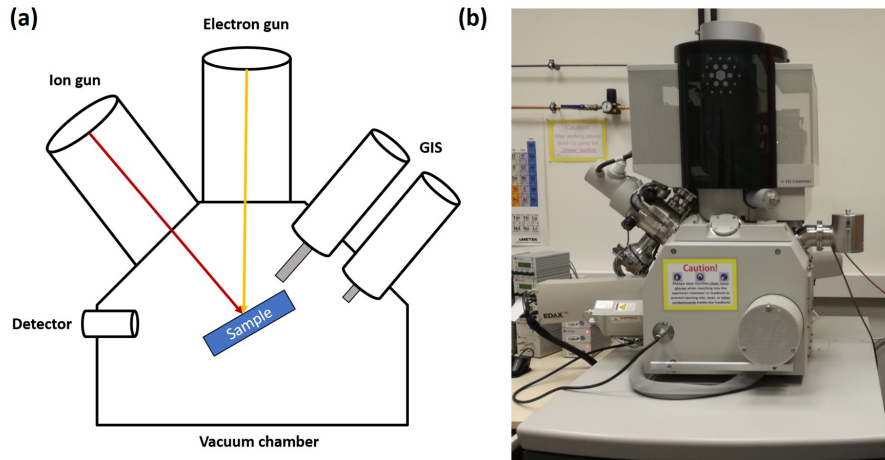
Figure 3.7: (a) Schematics of basic components of SEM/FIB systems: vacuum chamber, ion optical column, electron optical column, tilt stage and GIS. (b) Picture of SEM/FIB system.

digital computers, discrete problems can generally be solved easily even if the number of elements is very large. As the capacity of all computers is finite, for continuous problems the PDEs cannot be solved with analytical methods. Instead, an approximation of the equations can be constructed, typically based upon different types of *discretizations*. These discretization methods approximate the PDEs with numerical model equations, which can be solved using numerical methods. The solution to the numerical model equations approximates the real solution to the PDEs: the *finite element method* (FEM) is a tool to compute such approximations [81]. This method can be described as a general discretization procedure of continuum problems posed by mathematically defined statements. FEM is typically used to solve problems as for example structural analysis, heat transfer, fluid flow and mass transport.

3.5.1 FEM formulation

All analyses involving problems of discrete nature follow a standard methodology: first, the solution is computed for individual elements that compose the system, then the general solution is computed by assembling the whole system. The existence of a general patter applicable to all discrete systems allows to define a standard discrete problem. The FEM can be generally defined as an approximation process to continuum problems such that [82]:

(i) the continuum is divided into a finite number of parts (elements), the behaviour of which is specified by a finite number of parameters;

(ii) the solution of the complete system as an assembly of its elements follows precisely the same rules as those applicable to standard discrete problems.

Roughly speaking, the FEM formulation of the problem results in a system of algebraic equations, and the PDEs are approximated over the domain. To solve the problem, FEM subdivides a large continuous system into smaller and simpler parts, the so-called *finite elements*. The equations that model these finite elements are then assembled into a larger system of equations that describes the entire problem. FEM then uses variational methods to approximate a solution by minimizing an associated error function.

More precisely, instead of treating the PDEs in their classical formulation, the FEM formulation consists in describing the system using a so-called *weak formulation*, which takes the form of a variational equation in Hilbert or Banach spaces. The functional spaces are then discretized by replacing them with finite-dimensional subspaces of functions which are usually piecewise polynomials, or maps of them, with respect to the elements of a predetermined mesh (typically it consists in simplices, quadrilaterals, or hexahedra). This process allows to obtain a discretized formulation of the PDEs to be solved. It can easily be viewed as a system of equations which, for linear partial differential equations, is again linear [83].

Chapter 4

Two-points electrical contact measurements

In this chapter, the experimental technique used for two-points electrical contact measurements of single free standing GaAs NWs is presented. Using the two-terminal geometry, I have measured different properties of single NWs in their as-grown geometry. The results of this measurement are listed in this chapter. First, I have measured the conductivity of different NWs standing onto the same substrate, extracting the resistance of each NW using thermionic emission theory. Then, I have acquired the resistance profile of single NWs along the growth direction, comparing the experimental results with numerical calculations based upon FEM simulations. Finally, I have studied the correlation between mechanical stress applied to one NW with its electrical properties, using the W-probe to bend the NW applying different stresses.

4.1   Be-doped GaAs nanowires

The studied samples are (111)-oriented Be-doped GaAs NWs, with doping concentration of $10^{19} cm^{-3}$ grown on a Si(111) substrate by self-assisted growth in MBE, illustrated in section 1.1.2, in *Paul Drude Institute* in Berlin supervised by Dr. Lutz Geelhaar and Dr. Jesus Herranez. NWs have been grown on native oxide layer with diameters around 100 nm and height ranging from 10 µm to 20 µm.

I have performed the electrical characterization in a FIB/SEM chamber using nanometer-sized W-probes driven by two piezo-manipulators (Kleindiek, MM3A-EM [84]) to contact the conducting substrate and the single selected NW. The Si substrate has Ohmic behaviour due to the high dopant concentration. In order to provide Ohmic contacts to the back-side of single NWs, one of the W-probes is placed on the substrate after removing some material from oxide layer and depositing Pt layer instead using a Gas Injector System (GIS), as shown in figure 4.1.
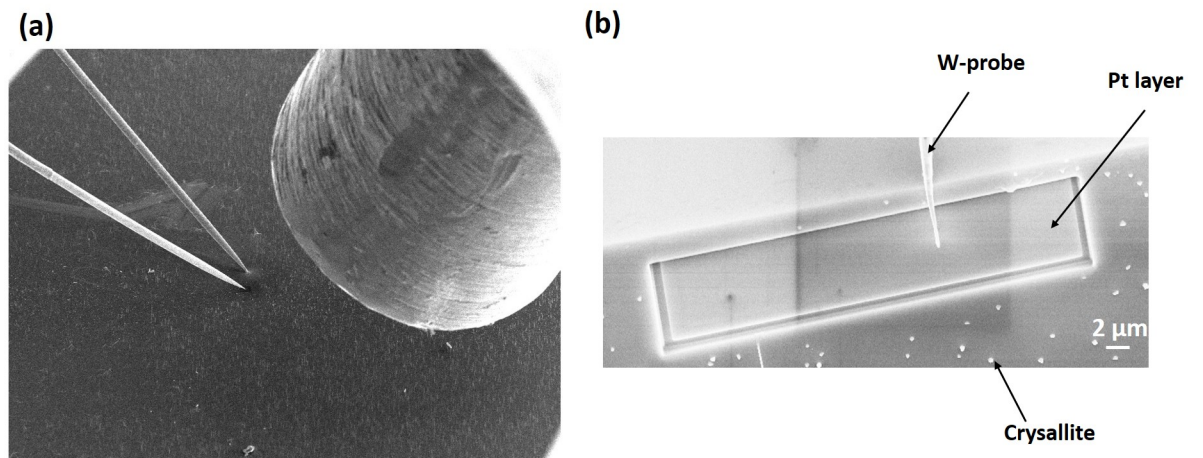
Figure 4.1: Tilted SEM images of (a) two W-probes and GIS needle for deposition of the Pt layer and (b) the deposited Pt layer after removal of the oxide layer on top of Si substrate.
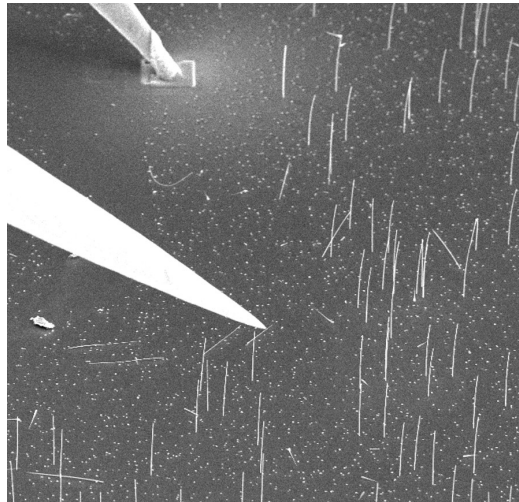
Figure 4.2: SEM images of the two terminal configuration: one W-tip is contacted to the Pt layer onto Si substrate, the other one on the single NW.

After turning-off the FIB and SEM, I-V characteristics are measured with a voltage varying between 0 V and +1 V, using a semiconductor analyzer instrument (Keithley 4200-SCS Parameter Analyzer [85]). Figure 4.2 represents the SEM image of two W-tips approaching the Pt layer on the substrate and the top of one selected NW.

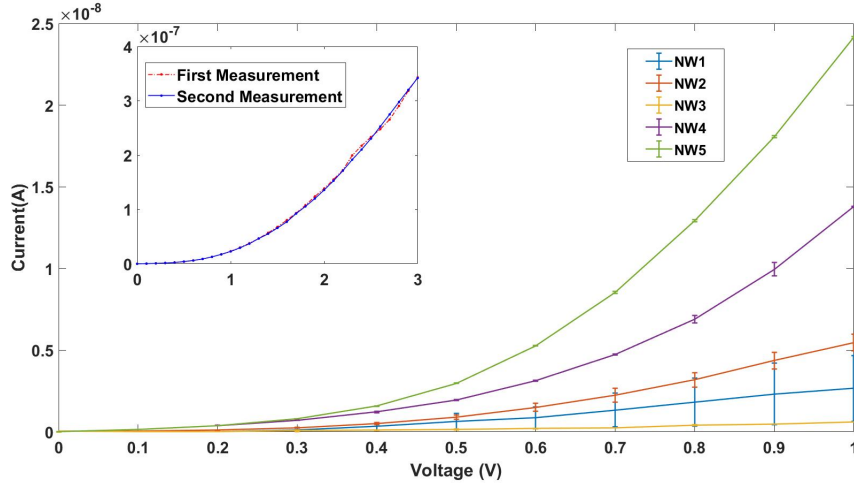Figure 4.3: I-V characteristics of five different single NWs all standing on the same Si substrate. (Inset) Example of the curves collected for a single NW for two consecutive contacting procedures: the curves are superimposed and no significant difference is observed.

4.2 Electrical resistance characterization of single GaAs nanowires

thermionic emission theory described in section 2.2.1 can be used in a back-to-back Schottky diode model to extract the resistance of some selected NWs. The measured system can in first approximation be described by two Schottky barriers embedding the NW. The two MS junctions are:

1. W-tip/NW

2. NW/highly n+ doped Si substrate

Thanks to the high doping level, the Si substrate is well described by a metal-like behaviour. The second junction can than be treated as a semiconductor/metal contact. This assumption reduces the contact between the Si substrate and the Pt contact to a simple metal/metal contact. According to the double Schottky diode model, the Schottky contact will be active at either the first or the second junction, depending on the sign of the applied voltage. When not active, one of the two Schottky diodes will have a resistive behaviour, with small values of the Schottky barrier, in series with the resistance of substrate, the active diode and the NW itself.

Figure 4.3 shows the I-V characteristics of different NWs on the same substrate: their shape follows the typical non-linear Schottky behaviour. The I-V characteristics of all NWs are obtained by repeating the measurement twice, and the mean current

is considered as the current passing through the wire. An example of the two curves obtained by repeating the top contact on the same NW are shown in the inset in figure 4.3. From the plot, we can deduce the reproducibility of the I-V measurements on the same NW. Half of the difference between two subsequent I-V measurement for each NW is calculated as the error of the experiment.

In a first approximation, the total current density is the same for the two diodes [1] formed by metal/semiconductor contacts, according to equation 2.9:

$$J_1 = J_2 = J = \frac{J_1 + J_2}{2} \tag{4.1}$$

and can be written as

$$J = A_{eff1,2} A^* T^2 exp(\frac{e\phi_{B1,2}}{kT}) exp(\frac{-e(V_{1,2} - R_s I)}{k_B T n_{ideality1,2}}) \tag{4.2}$$

where $A_{eff1,2}$ is the cross section of the NW in the (111) plane and the applied voltage V is shared between the two contacts, having values V_1 and V_2. A weighting parameter α ($0 < \alpha < 1$) is introduced, such that $V_1 = (1 - \alpha)V$ and $V_2 = \alpha V$, in order to quantify how the total voltage V is shared.

The experimental curves are fitted as shown in figure 4.4 to extract the values of parameters α, ϕ_{B1}, ϕ_{B2}, n_1 and n_2 and R_S. The fixed parameters used in the fit have the following values: $A^* = 4.4 \times 10^{-4} Am^{-2}K^{-2}$, $T = 300K$, $A_1 = \pi(90 \times 10^{-9})^2 m^2$ and $A_2 = \pi(25 \times 10^{-9})^2 m^2$. R_S represents the total series resistance of the whole system, i.e. the sum of the NW resistance (R_{NW}) and of the substrate and contact resistances (R_{ext}):

$$R_S = R_{NW} + R_{ext} \tag{4.3}$$

where

$$R_{ext} = R_{substrate} + R_{ohmiccontact} + R_{schottkycontact} \tag{4.4}$$

The substrate and the contact resistances are assumed to be similar for different NWs on the same substrate.

Repeating the resistance measurements for different NWs on the same substrate, very different values are obtained, as shown in table 4.1. The effective resistance is calculated for each NW as the ratio between the extracted resistance and the NW length. The effective resistance is then independent on the object length, and allows to compare the results between wires of different size.

Since the external parameters are all the same, the differences in resistance values depend on difference in conductivity between NWs.

These differences in electrical resistance of single NWs on the same substrate come from NW growth on native-Si oxide, which takes place at random positions on the

---

[1]diode 1 formed by W-tip/NW contact, diode 2 formed by NW/Si substrate contact.
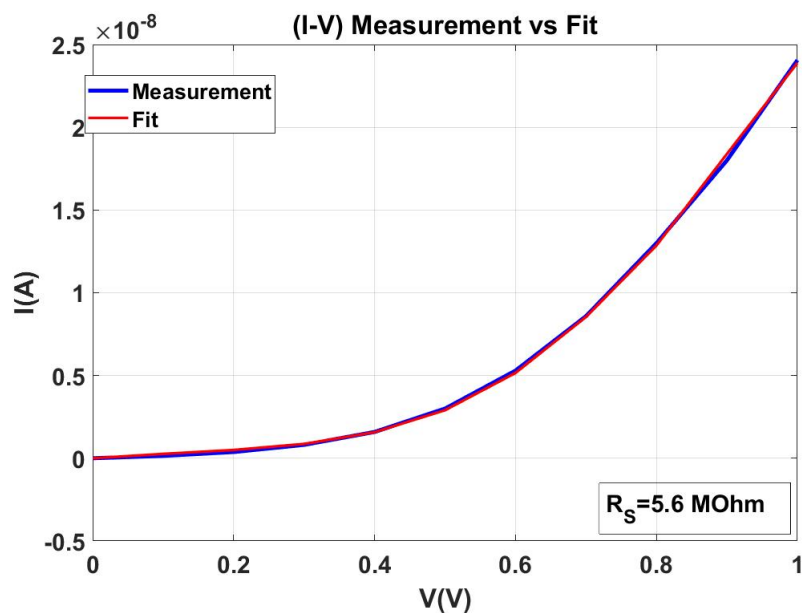
Figure 4.4: Results of the fitting of the electrical characteristic for a single GaAs NW in the range 0 V to +1 V (experimental data in blue and fit in red). $n_{1,2}$ and $\phi_{B1,2}$ are respectively the ideality factors and the barrier heights of the two diodes.

NW	$R_{eff} = R_S/\text{lenght}$ $(M\Omega/\mu m)$
NW1	$R_{eff} \simeq 3.6 \pm 0.1$
NW2	$R_{eff} \simeq 3.7 \pm 0.1$
NW3	$R_{eff} \simeq 1.8 \pm 0.1$
NW4	$R_{eff} \simeq 14.0 \pm 0.1$
NW5	$R_{eff} \simeq 0.4 \pm 0.1$
NW6	$R_{eff} \simeq 8.4 \pm 0.1$

Table 4.1: Extracted resistances for 6 different NWs on the same substrate

surface, leading to deviations of the local supply of source material at different NWs [86]. Consequently, the diameter, crystal phase structure, growth orientation and physical properties may differ comparing NWs grown on the same substrate. Another parameter which influences the NW conductivity is the dopant concentration. This parameter is different for each NW, because of the random nature of doping procedure. Then, NWs with higher doping concentration will have a lower resistance, and vice-versa. Other result of NW growth on native oxide layer is deviation in the contact area of single NWs to the substrate. Contact area of single GaAs NWs to Si substrate plays a crucial role in conductivity of these nano-objects.

4.3   FET geometry measurements

As mentioned above, the sample was grown in the *Paul Drude Institute* supervised by Dr. Lutz Geelhaar and Dr. Jesus Herranez. After growing the sample, they have characterized the NWs electrical conductivity using 4-point contact in FET geometry described in 4.3, as shown in picture 4.5 (a). The plot 4.5 (b) represents the I-V characteristics of different NWs belonging to the same sample, all obtained using the FET configuration.
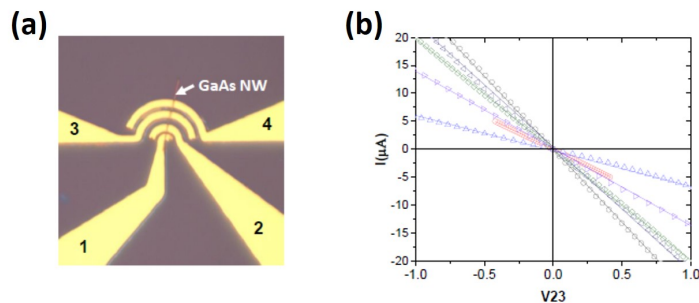

Figure 4.5: (a) Picture of the 4-point contact of a single NW in FET geometry. (b) I-V characteristics of different NWs grown under the same conditions.

Using this configuration, the resistances they have measured are in the range of $30/140\ k\Omega$, approximately three orders of magnitude lower than the resistances obtained characterizing free-standing NWs onto their growing substrate, in the range of $10/300$ $M\Omega$.

A first reason for this difference is related to the influence of the contact area on the effective resistance of free-standing NWs. A second cause of the higher resistance of NWs obtained from our measurements is the oxidation of NWs surface, causing a reduction in conductivity. What is more, not only the NWs but also the probes used for passing the current and measuring the voltage may be covered by an oxide layer, which lowers the current passing through the NW.

4.4   Current map along the side-wall of single nanowire

After the extraction of the resistance of the whole NW, the conductivity profile along the side-wall of single NW is investigated. The measurements are performed by contacting second W-probe to the side-wall of single NW and moving it along (from bottom to top). The I-V characteristic is recorded for each contact point. As it is shown from the graph in figure 4.6, the NW conductivity decreases as the tip is moved towards the top of NW. In order to compare size-independent results, the effective current passing through the NW at each different height is calculated as

$$I_{eff} = \frac{I}{height} \tag{4.5}$$

for each value of applied voltage. Using this procedure, we obtain a result free from the influence of the NW size: the differences in conductivity are then also related to other effects (e.g. the presence of interfaces or SFs), as explained below.
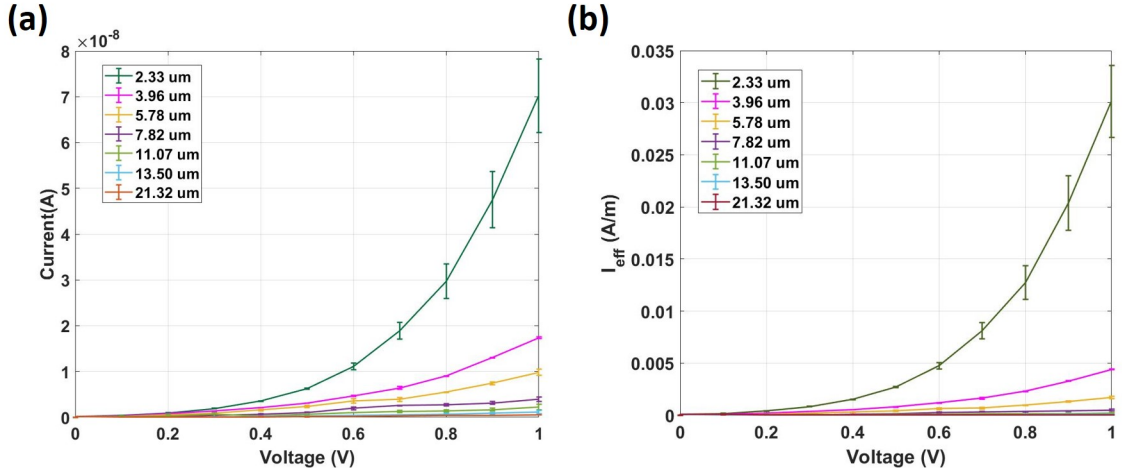

Figure 4.6: (a) I-V and (b) I_{eff}-V characteristics of the same NW acquired at different contact heights. The conductivity decreases as the W-tip is moved towards the top of the NW. The error bars are obtained by half the difference of two subsequent I-V measurements on the same contact point.

4.4.1   FEM simulations

To control our results, FEM calculations are performed to simulate I-V characteristics of the single NW. Our studied NWs are modeled using COMSOL Multiphysics [81] FEM based software. Two terminals are defined: one on the back-side of the NW by an ideal ohmic contact and the second one on the side-wall of the NW by an ideal Schottky

contact. Applying voltage to the second terminal at different heights along the side-wall of semiconductor NW and calculating the current, we could extract the I-V characteristics of the GaAs NW model as shown in figure 4.7.
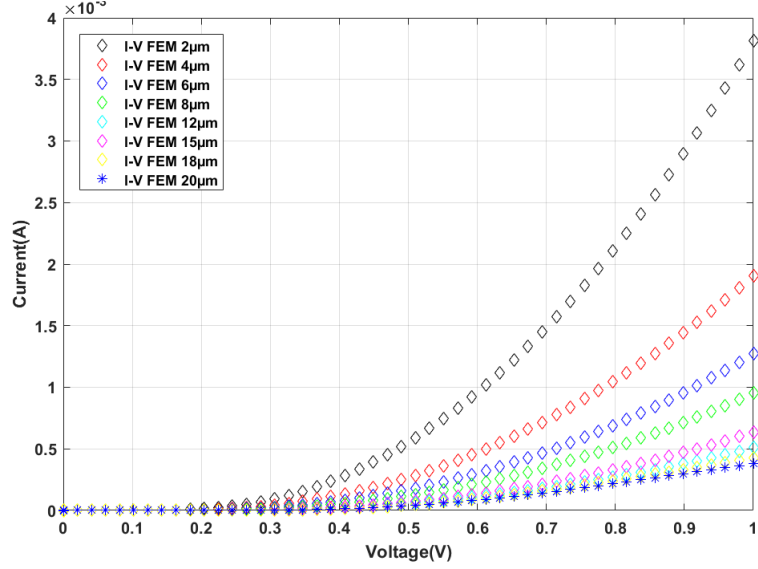

Figure 4.7: Simulated I-V characteristics of a NW with the same length as the measured one. The shape of the different curves are in agreement with the experimental results.

The measured and the simulated current map, with an applied voltage of +1 V, along the side-wall of NW are plotted respectively in figure 4.8a and 4.8b.

The shape of the experimental curves is in good agreement with the simulated ones. The differences in current values are related to ideality of the GaAs model compared to real system: simulations are performed considering the NW perfectly homogeneous and not oxidised, without any defect and fault and with ideal contacts in defined terminals.

4.4.2   Results and discussion

In order to compare size-independent results, the effective current passing through the NW with an applied voltage of +1 V is calculated as in equation 4.5. If the only parameter influencing the conductivity was the NW length, I_{eff} should be independent on the contact height, and then should be the same for each point. As highlighted by the plot in figure 4.9, the effective current decreases as the contact height is increased.

The measured decrease in electrical conductivity from bottom to top part of GaAs NW has direct correlation to the change in resistance volume which charge carriers face. On the other hand, we showed that the current passing through the NW does not only depend on the object's length. Another reason for the decrease in conductivity along the NW can be because of changing in the number of stacking faults existing along the
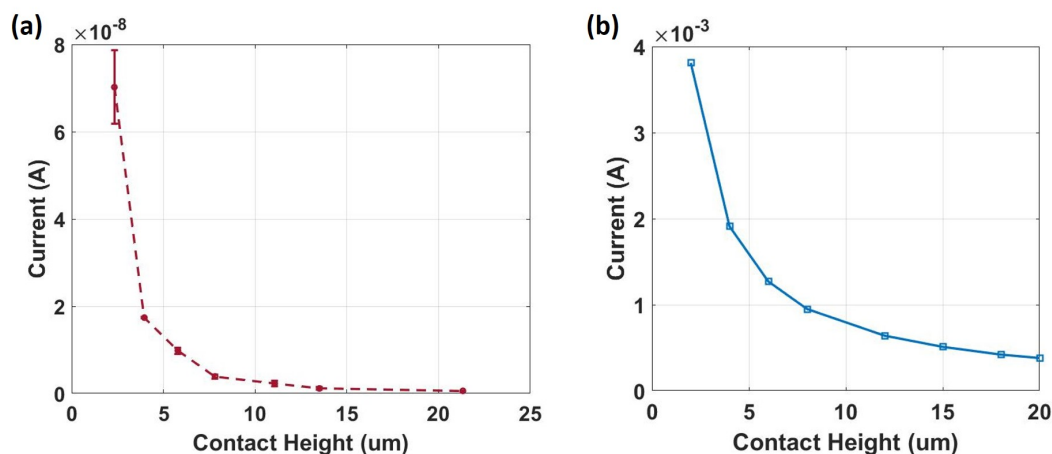
Figure 4.8: (a) Measured and (b) simulated current at applied voltage V = 1V as a function of contact height. The contact height is measured as the distance between the first probe and the substrate. The shapes of the two curves are close to each other. The strong difference in the current's order of magnitude is related to the fact that the GaAs NW used for simulations is an ideal model.

Figure 4.9: Effective current in logarithmic scale as a function of the contact height, measured as the tip/substrate distance. If the conductivity was only depending on the length, the effective current should be the same for each point.

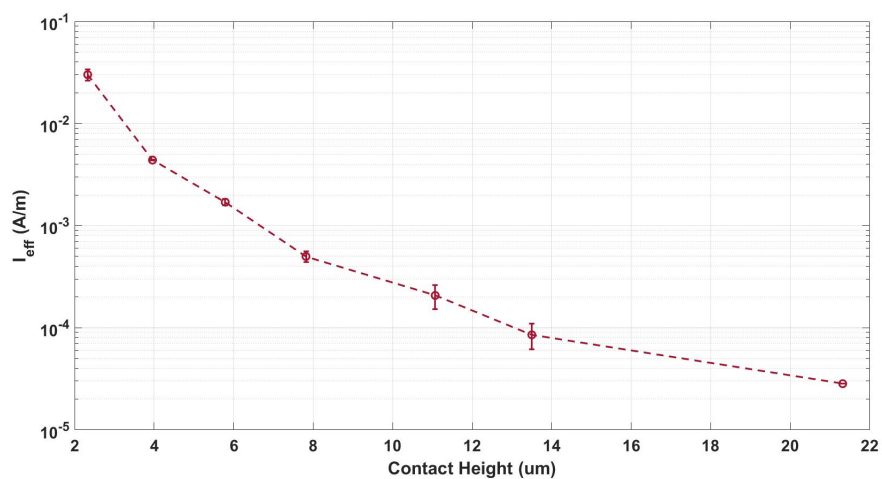growth direction, as it was studied previously by G. Bussone et al. [22]. What is more, also the crystalline structure changes along the NW. As explained in section 1.2 the crystal structure adopts different atomic configurations along the NW, e.g. the WZ and the ZB phase.

The presence of different crystalline phases introduces interfaces within the NW: the current is lower when charge carriers have to cross an interface. The sharp increase in current as the first probe is moved towards the bottom part of the NW is related to the number of interfaces the charge carriers have to cross to reach the substrate from the injecting probe. The closer is the tip to the substrate, the higher is the crystalline phase purity and the lower is the number of defects that the carriers meet through the NW. Then, the number of interfaces that charge carriers have to cross before reaching the substrate becomes lower as the tip is moved towards the bottom part of NW.

As demonstrated by the group of A. Biermanns [87], at the interface between the substrate and the NW there is residual strain which relaxes elastically. This strain relaxation exponentially decays with increasing of the NW height. The high density of defects at the NW/substrate interface can be explained by the small contact plane between the NW and substrate, while the NW grows radially on top of the oxide layer.

Besides the crystalline structure, also the dopant concentration is not uniform within the NW: charge carriers are passing through areas with different doping concentrations. The presence of regions with lower doping concentration clearly reduces the conductivity of the NW segment.

4.5   Conductivity of single nanowires under applied mechanical tension

In this section I will describe the effects of mechanical deformations of NWs on their conductivity. The analysis is performed by applying different mechanical stress to the same NW, using the W-probe contacted to the top part and acquiring the I-V characteristics at each different level of stress-induced deformation. The I-V curves as the function of mechanical stress are shown in figure 4.10 for a single GaAs NW. The plots show a strong increase in conductivity as the mechanical stress applied on the top of the NW is increased. In the inset of figure 4.10, the I-V characteristics of the highest mechanical stressed NW and the straight NW are plotted in logarithmic scale. We can observe that, with the same voltage applied, the current passing through the stressed NW (blue curve) is 3 or 4 orders of magnitude higher than in the straight one (red curve).

The experimental results are in good agreement with the results presented by the group of Alekseev et al. [88], shown in figure 4.11.
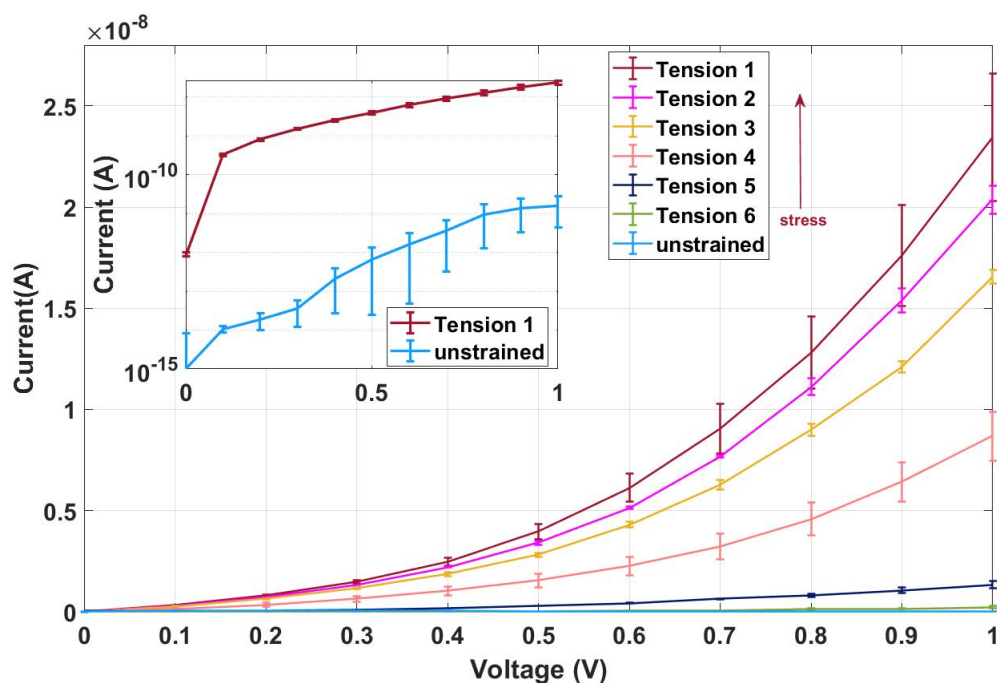
Figure 4.10: I-V characteristics of the same NW with different levels of applied stress. The curves are reported with decreasing level of applied stress, i.e. tension 1 is the highest one, while tension 8 corresponds to zero stress applied. The higher the applied strength, the higher the conductivity of the NW. (Inset) I-V characteristics in logarithmic scale of the most stressed NW (in blue) and of the straight one (in red).

Figure 4.11: I-V curves measured for different NW deformations produced by the lateral shift Δx of the AFM probe. Results from [88].

4.5.1   Discussion on the correlation between mechanical deformation and electrical conductivity

Because of the high surface/volume ratio, the conductivity of the GaAs NWs with an oxidized surface is governed mainly by surface states, that fix the surface Fe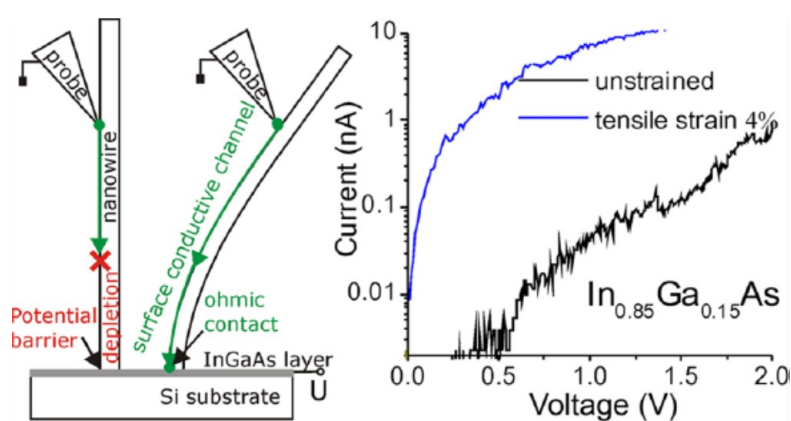rmi level near the mid-gap. This causes formation of near-surface depletion layer that narrows the conductive core and decreases the NW conductivity, as shown in figure 4.12.

Such pinning behaviour is assumed to be induced by a layer of As atoms forming at the NW surfaces because of incomplete oxidation of GaAs in ambient atmosphere. The increase in conductivity of NW with increasing strain can be explained through the stress-induced variations of the band structure. First, if the pinning of the Fermi level is induced by the surface As layer, the Fermi level position is mainly determined by the work function of the As layer. Then, the applied tension cannot shift the Fermi level position. However, the applied tension produces NW tensile strain, which generally shifts the conduction band minima (CMB) downward with respect to the vacuum level, reducing the initial potential barrier. If the CMB is moved below the Fermi level, this strain-induced downshift of CMB could lead to the formation of a surface conduction channel. As a result, the NW conductivity should increase significantly, as observed in the experimental data.

What is more, the application of mechanical stress to NWs cause the electrons to accumulate in certain regions. This accumulation makes the traveling of charge carriers easier in the strained NW, causing an increase in conductivity.

Using the setup we have used for the electrical characterization of strained NWs (i.e. the two-terminal configuration in a SEM/FIB dual beam chamber) it is impossible to quantify the applied strength. In the paper presented by Alekseev and his group [88], they have studied the effect of mechanical strain on the NW conductivity using C-AFM. In order to control the applied stress, they have proceeded as follows. Initially, the AFM probe touches the vertically standing NW in the upper part of the NW at a constant height $\Delta z = 500 nm$ (point A') from the NW base, while the circuit is closed by grounding
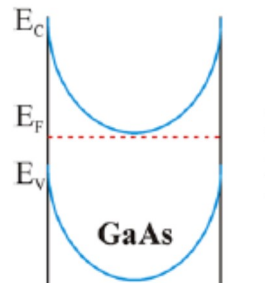

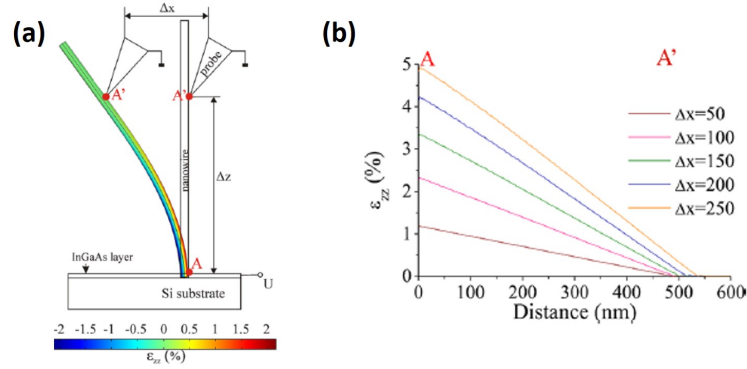Figure 4.12: Band structure of GaAs NWs with oxidized surfaces [88].

Figure 4.13: (a) Experimental configuration for measurements of the I-V curves for a strained NW by the AFM conductive probe (right) and corresponding strain distribution across the NW diameter at its base (left). In color scale, the strain at the NW base along its diameter calculated for $\Delta x = 100nm$. (b) Calculated distribution of the NW strain between the NW base and contact with the probe (point A') as a function of Δx [88].

the substrate. First, they have measured the I-V curve for the unstrained NW. Then, the conductivity measurements were repeated after successive equidistant ($\Delta x = 50nm$) displacements of the probe in the lateral direction. In order to characterize the NW strain (ϵ) induced by the probe shift Δx they have performed numerical simulations. The main contribution to the strain is produced by the ϵ_{zz} component. The result they have obtained using numerical simulations is shown in figure 4.13. The image 4.13 (a) represents the distribution of the strain at the NW base along its diameter calculated for $\Delta x = 100nm$. The important result from this analysis is that tensile strain is maximum at the NW surface from the side touching the probe. The plot 4.13 (b) demonstrates strain (ϵ_{zz}) profiles along the NW surface A-A' calculated for different lateral shifts of Δx. One can conclude that for all Δx values, the strain grows linearly from the NW base to the top.

4.6 Limitations of the 2-terminal configuration

The two-point setup provides reliable results on the electrical conductivity of single free standing NWs on their as-grown substrate. Furthermore, the measurements are relatively easy to be performed using a FIB/SEM dual beam system. However, this technique presents some limitations. First of all, the measured resistance is not only the resistance of the NW, but it also includes the substrate resistance as well as the contact resistances, as shown in equation 4.4. Secondly, it is not possible to control the contact area of single GaAs NWs to Si substrate. Since this parameter is suppose to influence the NW conductivity, with the two-terminal configuration we should also take into account

the differences in contact area between different NWs . Finally, using the two-terminal configuration, we must take into account the metal/semiconductor/metal interface which is created, and data must be treated using the thermionic emission theory. This makes the data fitting procedure complicated and, due to the large number of free parameters, not really precise.

To solve the limitations presented by the two-terminal configuration, the four-terminal configuration is a suitable technique for electrical resistance measurements. The measurements performed using this geometry will be described in the next chapter.

Chapter 5

Four-points electrical contact measurements

I have performed the four-terminal electrical measurements in the *Leibniz Universität Hannover* with the group of Prof. Dr. Christoph Tegenkamp and supervision of Dr. Frederik Edler. The sample characterized in this experiment is the same one used in the two-points measurements.

5.1   Experimental setup

The experiments are performed at room temperature by means of a commercial 4-tip STM system (from Omicron NanoScience [89]) in combination with a high-resolution (4 nm resolution) SEM column. To minimize the influence of defect adsorption, experiments are carried out in an ultra-clean environment under UHV conditions (pressure below $3 \times 10^{-10} mbar$). A schematic overview of the UHV chamber is given in figure 5.1. The chamber is separated into two parts: a preparation and an analysis chamber. Additionally, for every chamber part there are load lock chambers which allow the exchange of samples as well as the replacement of tips without compromising the UHV conditions. The main part of the analysis chamber is formed by a multi-tip STM in combination with a high resolution SEM, which allows the exact positioning of STM tips and contacting of nanostructures in the nm ranges.

Contacting procedure

Electrochemically etched W-wires are used as probe tips. A picture of the probes contacting the sample is shown in figure 5.2a, sketched in figure 5.2b. The sample is mounted with a 45° tilt, so that the NWs could be observed by SEM and three tips could be brought into contact with the same selected NW. The high-resolution SEM column al-
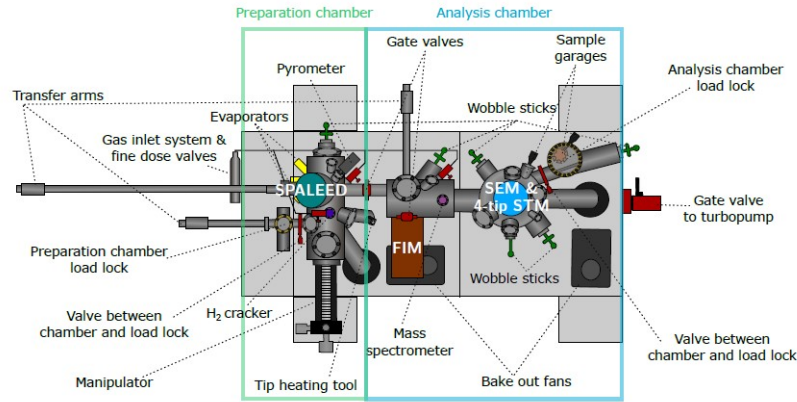
Figure 5.1: Schematic of the UHV chamber used for the 4-terminal conductivity measurements. The chamber is divided into two parts: preparation chamber and analysis chamber (4pp STM in combination with a SEM).

lows a precise navigation of the W-tip in proximity of the GaAs NW. The approaching procedure is explained below.

First, the tips are driven to their desired position on the substrate by controlling the movement by the SEM. Then, the tips are approached by the STM feedback loop to the specified tunnel current, in order to avoid irreversible damages to the probes. For transport measurements, the feedback loop is turned off and the tips are brought in contact to the sample surface in 0.1 nm steps. A 10 mV voltage is applied between the sample ground and the tip which is getting approached. When the measured current jumps from the noise level with blanked SEM beam ($\simeq 10^{-10}A$) to about $10^{-7}A$, it means a reliable contact is realized. Once the tip is landed onto the substrate, it is moved towards the bottom of the NW. Finally, the tip is moved along the side wall of the NW with the constant-current mode permanently active, until the desired position is reached. Here, electric contact is realized by a defined push-down of the tip using calibrated piezoelectric manipulators, in the feedback-off mode.

Using the procedure described above, three W-tips are accurately placed on the NW side walls, as shown in figure 5.3. The fourth tip is landed onto the Pt-layer deposited onto the Si substrate, as described in section 4.1.

The current is passed from the tip approaching the top of NW (tip 1) to the tip approaching the substrate (tip 4), and the voltage difference is measured between the two probes contacting the side wall of the NW (tips 2 and 3), avoiding the contact and the substrate resistances, as shown in figure 2.3. Due to the p-n junction between the p-doped NW and the n-doped substrate, a measurable current flows only in forward direction. Typically, a maximum current of 1 μA is applied, to avoid melting the NW. During the measurements, tips 2 and 3 contacted the NW along its length and measured
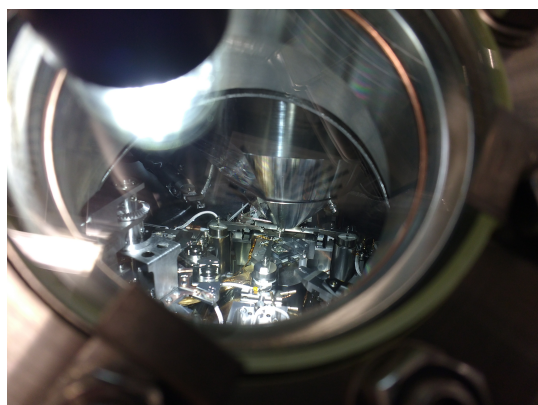
(a) Picture of the W-tips contacting the sample in the 4-tip-STM/SEM system.
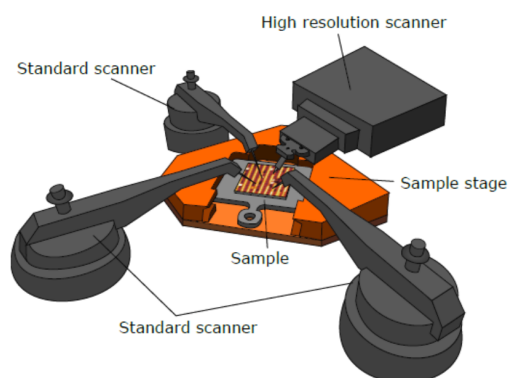
(b) Sketch of the probes contacting the sample.

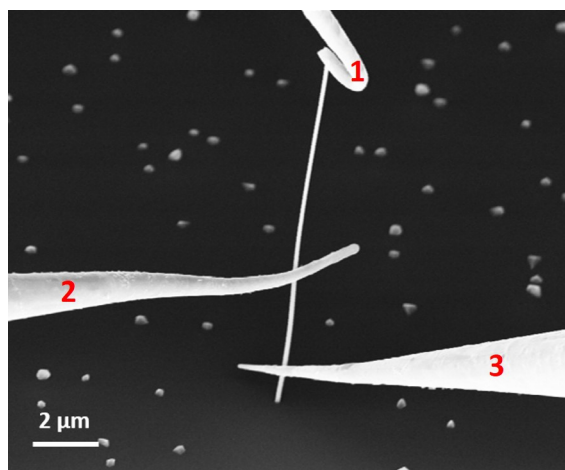Figure 5.2: Probes contacting the sample in a STM/SEM system.

Figure 5.3: SEM image of three W-probes approaching the selected NW. The fourth contact is used to close the circuit, contacting the substrate.

the potentials V_2 and V_3, in order to obtain the voltage drop $V_{23} = V_2 - V_3$ that occurred in between the contact points because of NW resistance. For measurements in this geometry, contrary to the two terminal configuration, we expect a linear shape of the resulting I-V_{23} curves. From the slope of this curve, the resistance R_{23} of the NW segment between the probes 2 and 3 can be calculated using a linear fit, excluding any influence of contact resistances between tips and NW. Sourcing and probing of currents and voltages is done by means of a Keithley sourcemeter [90].

5.2   Four-points contact measurements

The approaching of one single NW with three probes is challenging. It is necessary to use very high aspect ratio (i.e length/diameter). NWs, which are flexible and do not detach from the substrate too easily. The goal of our measurements is to obtain the resistance profile along the NW, by moving probe 2 along the side wall of the NW and keeping the other probes fixed. During the measurements, we had to face some geometrical and experimental problems which prevented us to reach this aim. A first problem is the inhomogeneous oxidation of single NW: the top part is almost not conductive because of the deposited oxide layer. To overcome this problem, we brought the top contact in the middle part of the NW, in order to acquire the I-V characteristic. The results of this measurement are plotted in figure 5.4.

The slope of the curve is obtained by a linear fit, and the reverse of the slope represents the resistance R_{23} of the NW segment between the voltage probe tips. For the measured NW, the calculated resistance is $R_{23} \simeq 8M\Omega$. The result we have obtained using the four-terminal configuration has the same order of magnitude of the resistances measured with the two-terminal geometry, presented in table 4.1, showing a compatibility of the results obtained with the two different techniques.

As mentioned above, during 4 terminal measurements we had to face some experimental and technical problems, which are listed below, with some possible solutions that can be adopted for future experiments.

- Surface oxidization of single NWs causes low conductivity. This problem can be solved with two different approaches. The first one is to substitute the sample, using a new array of NWs which should be kept under vacuum conditions to prevent GaAs to be oxidized. An alternative solution can be to remove the oxide layer from the sample using HF treatment, as in the work presented by Miccoli and its group [61]. They have cleaned the sample before loading it into the STM microscope by deep immersion in a low-concentrated HF solution. The sample is then immediately loaded within the UHV chamber to prevent re-oxidation of the GaAs NW surface.

- Surface oxidation of the probes causes low conductivity. Probes are made by tungsten, which can be easily oxidized in atmosphere conditions. To overcome this
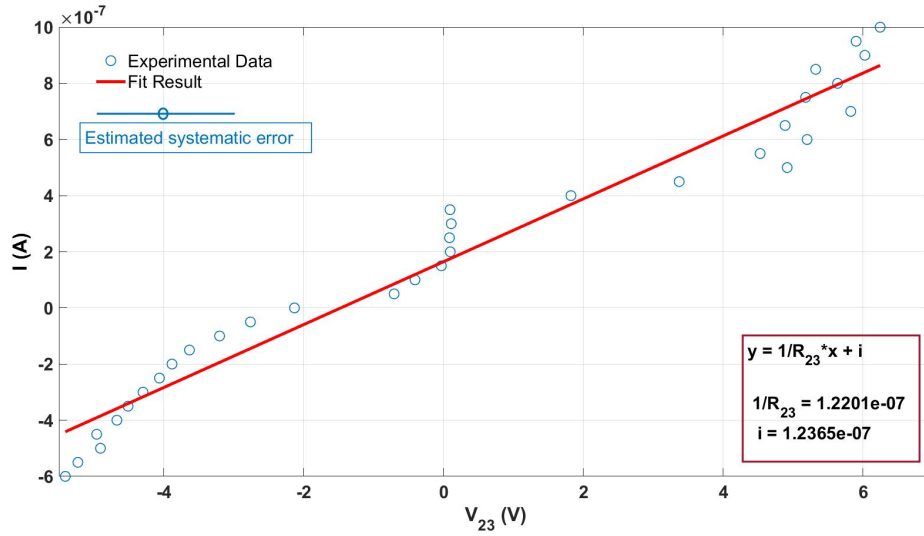
Figure 5.4: Results of the fitting of the electrical characteristic for a single GaAs NW (experimental data in blue and fit in red). In the textbox, the linear fit equation and parameters: the resistance of the NW segment between the voltage probe tips can be calculated as the reverse of the slope.

problem, tips can be covered by a layer of a noble metal (e.g. Au) to prevent oxidation. This approach was presented by G. A. Fried, X. D. Wang, and K. W. Hipps [91].

- As reported in section 4.1, part of the Si substrate was previously removed to deposit a Pt layer to increase the conductivity of the sample. Anyway, the sample within the chamber is tilted by 45°, and the probe approaching the substrate (probe 4) is parallel to the sample surface which causes lack of proper contact to Pt layer. If the Pt layer is not perfectly at the edges of the sample, the probe contacts the sample holder, which has low conductivity, causing a very low applied current. An alternative solution for this geometrical limitation is using Ag-glue deposition on the back of the sample and using the sample holder as the fourth contact provider.

Summary and conclusions

In this work, I presented electrical conductivity measurements on single GaAs NWs in their as-grown geometry in two different configurations.

I have shown that using two-point contacts reliable I-V characteristics can be extracted. Using thermionic emission theory, I could extract electrical resistance of single NWs. These results show that different NWs onto the same substrate have strongly different electrical properties mainly due to the different supply source material for different NWs grown on native oxide layer. Then, the current map along the side wall of single NWs is extracted. The conductivity of the NW decreases towards the top part of the NW because of increasing in the number of axial interfaces, the dependence of the elastic strain relaxation at the NW/substrate interface on the NW length and the differences in doping concentration within the NW. Finally, the conductivity of single NWs is studied as a function of the applied mechanical stress. The results show an increase of the NW conductivity with increasing of the applied tension, due to modifications of band structure and charge carrier density induced by the stress.

In order to measure the resistance of one single NW, two-point measurements have some disadvantages. The main limitation is due to the series resistance we measure with the NW resistance, i.e. the substrate resistance and contributions of contact and probe resistances. In order to overcome this problem, and to measure just the single NW resistance, I have repeated the electrical characterization using the four-terminal configuration. As I explained, this method has a lot of challenges. The oxidization of the NW surfaces and probes are the most important limitations for this configuration. The extracted results for electrical resistance of single NWs in this geometry are comparable with the results obtained in the two-point configuration. Therefore, a list of suggestions have been covered in order to improve the performances of this configuration for further investigations.

Bibliography

[1] R. Yan, D. Gargas, and P. Yang, "Nanowire photonics," *Nature Photonics*, vol. 3, pp. 569–576, Oct. 2009.

[2] C. K. Chan, H. Peng, G. Liu, K. McIlwrath, X. F. Zhang, R. A. Huggins, and Y. Cui, "High-performance lithium battery anodes using silicon nanowires," *Nature Nanotechnology*, vol. 3, pp. 31–35, Dec. 2007.

[3] F. Patolsky, G. Zheng, and C. M. Lieber, "Nanowire-based biosensors," *Analytical Chemistry*, vol. 78, pp. 4260–4269, July 2006.

[4] A. Milnes and A. Polyakov, "Indium arsenide: a semiconductor for high speed and electro-optical devices," *Materials Science and Engineering: B*, vol. 18, pp. 237–259, Apr. 1993.

[5] B. G., *Structure and electrical response of GaAs nanowires*. PhD thesis, Siegen University, 2015.

[6] "Explained: Nanowires and nanotubes." http://news.mit.edu/2013/explained-nanowires-and-nanotubes-0411.

[7] M. Meyyappan and M. K. Sunkara, *Inorganic Nanowires: Applications, Properties, and Characterization (Nanomaterials and their Applications)*. CRC Press, 2009.

[8] T. Ito and S. Okazaki, "Pushing the limits of lithography," *Nature*, vol. 406, pp. 1027–1031, Aug. 2000.

[9] K. A. Dick, "A review of nanowire growth promoted by alloys and non-alloying elements with emphasis on au-assisted III–v nanowires," *Progress in Crystal Growth and Characterization of Materials*, vol. 54, pp. 138–173, Sept. 2008.

[10] R. S. Wagner and W. C. Ellis, "VAPOR-LIQUID-SOLID MECHANISM OF SINGLE CRYSTAL GROWTH," *Applied Physics Letters*, vol. 4, pp. 89–90, Mar. 1964.

[11] V. G. Dubrovskii, N. V. Sibirev, J. C. Harmand, and F. Glas, "Growth kinetics and crystal structure of semiconductor nanowires," *Physical Review B*, vol. 78, Dec. 2008.

[12] A. Biermanns, S. Breuer, A. Davydok, L. Geelhaar, and U. Pietsch, "Structural polytypism and residual strain in gaas nanowires grown on si(111) probed by single-nanowire x-ray diffraction," *Journal of Applied Crystallography*, vol. 45, 04 2012.

[13] S. Breuer, C. Pfuller, T. Flissikowski, O. Brandt, H. T. Grahn, L. Geelhaar, and H. Riechert, "Suitability of au- and self-assisted GaAs nanowires for optoelectronic applications," *Nano Letters*, vol. 11, pp. 1276–1279, Mar. 2011.

[14] A. F. i Morral, C. Colombo, G. Abstreiter, J. Arbiol, and J. R. Morante, "Nucleation mechanism of gallium-assisted molecular beam epitaxy growth of gallium arsenide nanowires," *Applied Physics Letters*, vol. 92, p. 063112, Feb. 2008.

[15] C. Colombo, D. Spirkoska, M. Frimmer, G. Abstreiter, and A. F. i Morral, "Ga-assisted catalyst-free growth mechanism of GaAs nanowires by molecular beam epitaxy," *Physical Review B*, vol. 77, Apr. 2008.

[16] M. H. Madsen, M. Aagesen, P. Krogstrup, C. Sørensen, and J. Nygård, "Influence of the oxide layer for growth of self-assisted InAs nanowires on si(111)," *Nanoscale Research Letters*, vol. 6, Aug. 2011.

[17] F. Matteini, G. Tütüncüoğlu, D. Rüffer, E. Alarcón-Lladó, and A. F. i Morral, "Ga-assisted growth of GaAs nanowires on silicon, comparison of surface SiOx of different nature," *Journal of Crystal Growth*, vol. 404, pp. 246–255, Oct. 2014.

[18] K. Tomioka, M. Yoshimura, and T. Fukui, "A III–v nanowire channel on silicon for high-performance vertical transistors," *Nature*, vol. 488, pp. 189–192, Aug. 2012.

[19] A. M. Munshi, D. L. Dheeraj, V. T. Fauske, D. C. Kim, J. Huh, J. F. Reinertsen, L. Ahtapodov, K. D. Lee, B. Heidari, A. T. J. van Helvoort, B. O. Fimland, and H. Weman, "Position-controlled uniform GaAs nanowires on silicon using nanoimprint lithography," *Nano Letters*, vol. 14, pp. 960–966, Jan. 2014.

[20] J. D., *Crystal Structure Determination of III-V nanowires*. PhD thesis, Lund University, 2013.

[21] D. Kriegner, C. Panse, B. Mandl, K. A. Dick, M. Keplinger, J. M. Persson, P. Caroff, D. Ercolani, L. Sorba, F. Bechstedt, J. Stangl, and G. Bauer, "Unit cell structure of crystal polytypes in InAs and InSb nanowires," *Nano Letters*, vol. 11, pp. 1483–1489, Apr. 2011.

[22] G. Bussone, H. Schäfer-Eberwein, E. Dimakis, A. Biermanns, D. Carbone, A. Tahraoui, L. Geelhaar, P. H. Bolívar, T. U. Schülli, and U. Pietsch, "Correlation of electrical and structural properties of single as-grown GaAs nanowires on si (111) substrates," *Nano Letters*, vol. 15, pp. 981–989, Jan. 2015.

[23] P. Yang, R. Yan, and M. Fardy, "Semiconductor nanowire: What's next?," *Nano Letters*, vol. 10, pp. 1529–1536, May 2010.

[24] H. Zhu, J. E. Bonevich, H. Li, C. A. Richter, H. Yuan, O. Kirillov, and Q. Li, "Discrete charge states in nanowire flash memory with multiple ta2o5 charge-trapping stacks," *Applied Physics Letters*, vol. 104, p. 233504, June 2014.

[25] L.-E. Wernersson, T. Bryllert, E. Lind, and L. Samuelson, "Wrap-gated inas nanowire field-effect transistor," in *IEEE InternationalElectron Devices Meeting, 2005. IEDM Technical Digest.*, IEEE.

[26] H. Haick, P. T. Hurley, A. I. Hochbaum, P. Yang, and N. S. Lewis, "Electrical characteristics and chemical stability of non-oxidized, methyl-terminated silicon nanowires," *Journal of the American Chemical Society*, vol. 128, pp. 8990–8991, July 2006.

[27] Y. Imai, M. Sato, T. Tanaka, S. Kasai, Y. Hagiwara, H. Ishizaki, S. Kuwabara, and T. Arakawa, "Detection of weak biological signal utilizing stochastic resonance in a GaAs-based nanowire FET and its parallel summing network," *Japanese Journal of Applied Physics*, vol. 53, p. 06JE01, May 2014.

[28] A. Kolmakov, Y. Zhang, G. Cheng, and M. Moskovits, "Detection of CO and o2 using tin oxide nanowire sensors," *Advanced Materials*, vol. 15, pp. 997–1000, June 2003.

[29] Y. Cui, "Nanowire nanosensors for highly sensitive and selective detection of biological and chemical species," *Science*, vol. 293, pp. 1289–1292, Aug. 2001.

[30] M.-W. Shao, Y.-Y. Shan, N.-B. Wong, and S.-T. Lee, "Silicon nanowire sensors for bioanalytical applications: Glucose and hydrogen peroxide detection," *Advanced Functional Materials*, vol. 15, pp. 1478–1482, Sept. 2005.

[31] M. Law, "Nanoribbon waveguides for subwavelength photonics integration," *Science*, vol. 305, pp. 1269–1273, Aug. 2004.

[32] X. Duan, Y. Huang, R. Agarwal, and C. M. Lieber, "Single-nanowire electrically driven lasers," *Nature*, vol. 421, pp. 241–245, Jan. 2003.

[33] C. Hahn, Z. Zhang, A. Fu, C. H. Wu, Y. J. Hwang, D. J. Gargas, and P. Yang, "Epitaxial growth of InGaN nanowire arrays for light emitting diodes," *ACS Nano*, vol. 5, pp. 3970–3976, Apr. 2011.

[34] P. Krogstrup, H. I. Jørgensen, M. Heiss, O. Demichel, J. V. Holm, M. Aagesen, J. Nygard, and A. F. i Morral, "Single-nanowire solar cells beyond the shockley–queisser limit," *Nature Photonics*, vol. 7, pp. 306–310, Mar. 2013.

[35] I. Aberg, G. Vescovi, D. Asoli, U. Naseem, J. P. Gilboy, C. Sundvall, A. Dahlgren, K. E. Svensson, N. Anttu, M. T. Bjork, and L. Samuelson, "A GaAs nanowire array solar cell with 15.3% efficiency at 1 sun," *IEEE Journal of Photovoltaics*, vol. 6, pp. 185–190, Jan. 2016.

[36] Z. L. Wang, "Piezoelectric nanostructures: From growth phenomena to electric nano-generators," *MRS Bulletin*, vol. 32, pp. 109–116, Feb. 2007.

[37] M. Grundmann, *The physics of semiconductors: An introduction including devices and nanophysics*. 01 2006.

[38] L. Rigutti, G. Jacopin, L. Largeau, E. Galopin, A. D. L. Bugallo, F. H. Julien, J.-C. Harmand, F. Glas, and M. Tchernycheva, "Correlation of optical and structural properties of GaN/AlN core-shell nanowires," *Physical Review B*, vol. 83, Apr. 2011.

[39] K. Haraguchi, T. Katsuyama, and K. Hiruma, "Polarization dependence of light emitted from GaAsp-njunctions in quantum wire crystals," *Journal of Applied Physics*, vol. 75, pp. 4220–4225, Apr. 1994.

[40] R. Wang, H. P. T. Nguyen, A. T. Connie, J. Lee, I. Shih, and Z. Mi, "Color-tunable, phosphor-free ingan nanowire light-emitting diode arrays monolithically integrated on silicon," *Opt. Express*, vol. 22, pp. A1768–A1775, Dec 2014.

[41] P. Flewitt and R. Wild, *Physical Methods for Materials Characterisation*. United Kingdom: Institute of Physics, 1994.

[42] "Lasers* * light amplification by stimulated emission of radiation." `https://slideplayer.com/slide/4665714/`.

[43] S. W. Eaton, A. Fu, A. B. Wong, C.-Z. Ning, and P. Yang, "Semiconductor nanowire lasers," *Nature Reviews Materials*, vol. 1, May 2016.

[44] M. H. Huang, "Room-temperature ultraviolet nanowire nanolasers," *Science*, vol. 292, pp. 1897–1899, June 2001.

[45] B. Mayer, D. Rudolph, J. Schnell, S. Morkötter, J. Winnerl, J. Treu, K. Müller, G. Bracher, G. Abstreiter, G. Koblmüller, and J. J. Finley, "Lasing from individual GaAs-AlGaAs core-shell nanowires up to room temperature," *Nature Communications*, vol. 4, Dec. 2013.

[46] A. Nagelein, C. Timm, M. Steidl, P. Kleinschmidt, and T. Hannappel, "Multi-probe electrical characterization of nanowires for solar energy conversion," *IEEE Journal of Photovoltaics*, vol. 9, pp. 673–678, May 2019.

[47] C. Colombo, M. Heiβ, M. Grätzel, and A. F. i Morral, "Gallium arsenide p-i-n radial structures for photovoltaic applications," *Applied Physics Letters*, vol. 94, p. 173108, Apr. 2009.

[48] P. Hiralal, H. E. Unalan, and G. A. J. Amaratunga, "Nanowires for energy generation," *Nanotechnology*, vol. 23, p. 194002, Apr. 2012.

[49] M. Minary-Jolandan, R. A. Bernal, I. Kuljanishvili, V. Parpoil, and H. D. Espinosa, "Individual GaN nanowires exhibit strong piezoelectricity in 3d," *Nano Letters*, vol. 12, pp. 970–976, Jan. 2012.

[50] P. Kusch, S. Breuer, M. Ramsteiner, L. Geelhaar, H. Riechert, and S. Reich, "Band gap of wurtzite GaAs: A resonant raman study," *Physical Review B*, vol. 86, Aug. 2012.

[51] A. Casadei, J. Schwender, E. Russo-Averchi, D. Rüffer, M. Heiss, E. Alarcó-Lladó, F. Jabeen, M. Ramezani, K. Nielsch, and A. F. i Morral, "Electrical transport in c-doped GaAs nanowires: surface effects," *physica status solidi (RRL) - Rapid Research Letters*, vol. 7, pp. 890–893, May 2013.

[52] T. B. Hoang, A. F. Moses, L. Ahtapodov, H. Zhou, D. L. Dheeraj, A. T. J. van Helvoort, B.-O. Fimland, and H. Weman, "Engineering parallel and perpendicular polarized photoluminescence from a single semiconductor nanowire by crystal phase control," *Nano Letters*, vol. 10, pp. 2927–2933, Aug. 2010.

[53] N. P. Dasgupta, J. Sun, C. Liu, S. Brittman, S. C. Andrews, J. Lim, H. Gao, R. Yan, and P. Yang, "25th anniversary article: Semiconductor nanowires - synthesis, characterization, and applications," *Advanced Materials*, vol. 26, pp. 2137–2184, Mar. 2014.

[54] D. Spirkoska, J. Arbiol, A. Gustafsson, S. Conesa-Boj, F. Glas, I. Zardo, M. Heigoldt, M. H. Gass, A. L. Bleloch, S. Estrade, M. Kaniber, J. Rossler, F. Peiro, J. R. Morante, G. Abstreiter, L. Samuelson, and A. F. i Morral, "Structural and optical properties of high quality zinc-blende/wurtzite GaAs nanowire heterostructures," *Physical Review B*, vol. 80, Dec. 2009.

[55] C. Thelander, P. Caroff, S. Plissard, A. W. Dey, and K. A. Dick, "Effects of crystal phase mixing on the electrical properties of InAs nanowires," *Nano Letters*, vol. 11, pp. 2424–2429, June 2011.

[56] A. D. Schricker, F. M. Davidson, R. J. Wiacek, and B. A. Korgel, "Space charge limited currents and trap concentrations in GaAs nanowires," *Nanotechnology*, vol. 17, pp. 2681–2688, May 2006.

[57] Y. Huang, X. Duan, Y. Cui, and C. M. Lieber, "Gallium nitride nanowire nanodevices," *Nano Letters*, vol. 2, pp. 101–104, Feb. 2002.

[58] A. A. Talin, F. Léonard, A. M. Katzenmeyer, B. S. Swartzentruber, S. T. Picraux, M. E. Toimil-Molares, J. G. Cederberg, X. Wang, S. D. Hersee, and A. Rishinaramangalum, "Transport characterization in nanowires using an electrical nanoprobe," *Semiconductor Science and Technology*, vol. 25, p. 024015, Jan. 2010.

[59] O. Wunnicke, "Gate capacitance of back-gated nanowire field-effect transistors," *Applied Physics Letters*, vol. 89, p. 083102, Aug. 2006.

[60] D. R. Khanal and J. Wu, "Gate coupling and charge distribution in nanowire field effect transistors," *Nano Letters*, vol. 7, pp. 2778–2783, Sept. 2007.

[61] I. Miccoli, F. Edler, H. Pfnur, C. Tegenkamp, P. Prete, and N. Lovergine, "Surface-mediated electrical transport in single GaAs nanowires," in *2015 1st Workshop on Nanotechnology in Instrumentation and Measurement (NANOFIM)*, IEEE, July 2015.

[62] S. Sze and K. K. Ng, *Physics of Semiconductor Devices*. John Wiley & Sons, Inc., Apr. 2006.

[63] A. Cavallini and L. Polenta, "Electrical characterization of nanostructures," in *Characterization of Semiconductor Heterostructures and Nanostructures*, pp. 55–91, Elsevier, 2008.

[64] S. Mott, N. F. (Nevill Francis) and R. W. R. W. Gurney, *Electronic processes in ionic crystals*. Oxford : Clarendon Press, 2nd ed ed., 1948. Includes bibliography.

[65] E. H. Rhoderick and R. H. Williams, *Metal-Semiconductor Contacts (Monographs in Electrical and Electronic Engineering)*. Oxford University Press, 1988.

[66] Z. Zhang, K. Yao, Y. Liu, C. Jin, X. Liang, Q. Chen, and L.-M. Peng, "Quantitative analysis of current-voltage characteristics of semiconducting nanowires: Decoupling of contact effects," *Advanced Functional Materials*, vol. 17, pp. 2478–2489, Aug. 2007.

[67] S. K. Cheung and N. W. Cheung, "Extraction of schottky diode parameters from forward current-voltage characteristics," *Applied Physics Letters*, vol. 49, pp. 85–87, July 1986.

[68] M. A. Herman and H. Sitter, *Molecular Beam Epitaxy: Fundamentals and Current Status (Springer Series in Materials Science Book 7)*. Springer, 2012.

[69] J. Puebla, *Spin phenomena in semiconductor quantum dots*. PhD thesis, 10 2012.

[70] "SEM Technology Overview – Scanning Electron Microscopy ." `https://www.nanoimages.com/sem-technology-overview/`.

[71] "Electron Interaction with Matter." `https://en.wikipedia.org/wiki/Electron_microscope#/media/File:Electron_Interaction_with_Matter.svg`.

[72] J. I. Goldstein, D. E. Newbury, J. R. Michael, N. W. Ritchie, J. H. J. Scott, and D. C. Joy, *Scanning Electron Microscopy and X-Ray Microanalysis*. Springer New York, 2018.

[73] L. Reimer, *Scanning Electron Microscopy*. Springer Berlin Heidelberg, 1998.

[74] G. Binnig and H. Rohrer, "Scanning tunneling microscopy," *Surface Science*, vol. 126, pp. 236–244, Mar. 1983.

[75] C. J. Chen, *Introduction to Scanning Tunneling Microscopy*. Oxford University Press, Sept. 2007.

[76] B. Voigtländer, *Scanning Probe Microscopy*. Springer Berlin Heidelberg, 2015.

[77] J. Gierak, "Focused ion beam nano-patterning from traditional applications to single ion implantation perspectives," *Nanofabrication*, vol. 1, 02 2014.

[78] M. Y. Ali, W. Hung, and F. Yongqi, "A review of focused ion beam sputtering," *International Journal of Precision Engineering and Manufacturing*, vol. 11, pp. 157–170, Feb. 2010.

[79] J. Orloff, M. Utlaut, and L. W. Swanson, "High resolution focused ion beams: Fib and its applications," *Physics Today*, vol. 57, 01 2003.

[80] "Using FIB Secondary Ion Images to Observe the Presence of Corrosion." `http://www.fibics.com/fib/application/using-fib-secondary-ion-images-to-observe-the-presence-of-corrosion-/22/`.

[81] "The Finite Element Method (FEM)." `https://www.comsol.it/multiphysics/finite-element-method`.

[82] O. C. Zienkiewicz, R. L. Taylor, and J. Zhu, *The Finite Element Method: Its Basis and Fundamentals, Sixth Edition*. Butterworth-Heinemann, 2005.

[83] C. Hofreither, *A Non-standard Finite Element Method using Boundary Integral Operators*. PhD thesis, 12 2012.

[84] "Micromanipulator for Electron Microscopy." `https://www.nanotechnik.com/mm3a-em.html`.

[85] "Keithley 4200A-SCS Parameter Analyzer." `https://www.tek.com/keithley-4200a-scs-parameter-analyzer`.

[86] A. F. i. Morral, "Gold-free gaas nanowire synthesis and optical properties," *IEEE Journal of Selected Topics in Quantum Electronics*, vol. 17, pp. 819–828, July 2011.

[87] B. A., *X-ray diffraction from single GaAs nanowires*. PhD thesis, Siegen University, 2012.

[88] P. A. Alekseev, V. A. Sharov, M. S. Dunaevskiy, D. A. Kirilenko, I. V. Ilkiv, R. R. Reznik, G. E. Cirlin, and V. L. Berkovits, "Control of conductivity of InxGa1–xAs nanowires by applied tension and surface states," *Nano Letters*, vol. 19, pp. 4463–4469, June 2019.

[89] "ScientaOmicron." `https://www.scientaomicron.com/en/home`.

[90] "Keithley source measure units." `https://www.tek.com/keithley-source-measure-units`.

[91] G. A. Fried, X. D. Wang, and K. W. Hipps, "Gold-coated tungsten tips for scanning tunneling microscopy," *Review of Scientific Instruments*, vol. 64, pp. 1495–1501, June 1993.